

Helicity amplitudes in light-cone and Feynman-diagram gauges

Junmou Chen^{1,a}, Kaoru Hagiwara^{2,3b}, Junichi Kanzaki^{4,c}, Kentarou Mawatari^{5,d}, and Ya-Juan Zheng^{5,6,e}

¹ Department of Physics, Jinan University, Guangzhou, Guangdong Province, 510632, China

² Center for Theory and Computation, National Tsing Hua University, Hsinchu, Taiwan 300

³ KEK Theory Center and Sokendai, Tsukuba, Ibaraki 305-0801, Japan

⁴ Kavli IPMU (WPI), UTIAS, The University of Tokyo, Kashiwa, Chiba 277-8583, Japan

⁵ Faculty of Education, Iwate University, Morioka, Iwate 020-8550, Japan

⁶ Department of Physics and Astronomy, University of Kansas, Lawrence, KS 66045, U.S.A.

Abstract. Recently proposed Feynman-diagram (FD) gauge propagator for massless and massive gauge bosons is obtained from a light-cone (LC) gauge propagator, by choosing the gauge vector along the opposite direction of the gauge boson three-momentum. We implement a general LC gauge propagator for all the gauge bosons of the Standard Model (SM) in the HELicity Amplitude Subroutines (HELAS) codes, such that all the SM helicity amplitudes can be evaluated at the tree level in the LC gauge by using MadGraph. We confirm that our numerical codes produce physical helicity amplitudes which are consistent among all gauge choices. We then study interference patterns among Feynman amplitudes, for a few $2 \rightarrow 3$ scattering processes in QED and QCD, and the process $\gamma\gamma \rightarrow W^+W^-$ followed by the W^\pm decays. We find that in a generic LC gauge, where all the gauge boson propagators share a common gauge vector, we cannot remove the off-shell current components which grow with their energy systematically from all the Feynman amplitudes in $2 \rightarrow 3$ processes. On the other hand, the 5×5 LC gauge propagator for the weak bosons removes components which grow with energy due to the longitudinal polarization mode of the external bi-fermion currents, and hence can give $2 \rightarrow 2$ weak boson scattering amplitudes which are free from subtle cancellation at high energies. The particular choice of the FD gauge vector has advantages over generic LC gauge, not only because all the terms which grow with energy of off-shell and on-shell currents are removed systematically from all the diagrams, but also because no artificial gauge vector direction dependence of individual amplitudes appears.

1 Introduction

It has been shown recently [1, 2] that the tree-level scattering amplitudes of the Standard Model (SM) can be expressed in a form which is free from subtle gauge theory cancellation among interfering Feynman diagrams. The specific form of the gauge boson propagators which appear in the amplitudes are called ‘Feynman Diagram (FD)’ gauge [2], since the helicity amplitudes corresponding to individual Feynman diagram are expressed as products of the invariant Feynman’s propagator factors, for the connecting lines, and the ‘splitting amplitudes’ [3] at each vertex¹. Splitting amplitudes in the Electroweak (EW) theory for the weak bosons and the Higgs boson are found e.g. in refs. [4, 5], where the FD gauge propagators for the weak bosons are obtained [6] along studies of the Goldstone boson equivalence theorem [7, 8].

In refs. [1, 2], the FD gauge propagators are obtained from the scattering amplitudes expressed in a covariant

gauge, Feynman or Landau gauge in QED and QCD [1], or the Unitary gauge in the EW theory [2]. In case of the Landau gauge, the polarization tensor of the gauge boson propagator

$$P_{j=1}^{\mu\nu} = -g^{\mu\nu} + \frac{q^\mu q^\nu}{q^2} \quad (1)$$

can be expressed as a summation over the polarization vectors of definite helicities

$$P_{j=1}^{\mu\nu} = \sum_{h=\pm 1} \epsilon^\mu(q, h) \epsilon^\nu(q, h)^* + \text{sgn}(q^2) \epsilon^\mu(q, 0) \epsilon^\nu(q, 0). \quad (2)$$

The FD gauge propagator is obtained by noting that the longitudinal polarization vector can be expressed as a sum of the scalar term and the difference

$$\epsilon^\mu(q, 0) = \frac{q^\mu}{Q} + \tilde{\epsilon}^\mu(q, 0), \quad (3)$$

¹ Because of this property, the authors of ref. [1] called their photon and the gluon propagators as ‘Parton Shower (PS) gauge’. Since the term ‘PS gauge’ had been used in the parton shower studies [9, 10], we adopt the naming ‘FD gauge’, following ref. [2]

^a chenjm@jnu.edu.cn

^b kaoru.hagiwara@kek.jp

^c junichi.kanzaki@ipmu.jp

^d mawatari@iwate-u.ac.jp

^e yjzheng@iwate-u.ac.jp

where $Q = \sqrt{q^2}$ is the virtuality of the photon or gluon. Inserting eq.(3) into eq.(2), and dropping all terms proportional to q^μ or q^ν , by applying the BRST identities [11,12] for the sub-amplitudes with only one off-shell gauge boson, we arrive at the polarization tensor of the FD gauge:

$$P_{\text{FD}}^{\mu\nu} = \sum_{h=\pm 1} \epsilon^\mu(q, h) \epsilon^\nu(q, h)^* + \text{sgn}(q^2) \tilde{\epsilon}^\mu(q, 0) \tilde{\epsilon}^\nu(q, 0). \quad (4)$$

In case of the EW theory, we start from the amplitudes in the Unitary gauge of the weak bosons, whose polarization tensor

$$P_{\text{U}}^{\mu\nu}(V) = -g^{\mu\nu} + \frac{q^\mu q^\nu}{m_V^2} \quad (5)$$

for $V = W^\pm$ or Z can be expressed as [2]

$$P_{\text{U}}^{\mu\nu}(V) = \sum_{h=\pm 1} \epsilon^\mu(q, h) \epsilon^\nu(q, h)^* + \text{sgn}(q^2) \tilde{\epsilon}^\mu(q, 0) \tilde{\epsilon}^\nu(q, 0) + \tilde{\epsilon}^\mu(q, 0) \frac{q^\nu}{Q} + \frac{q^\mu}{Q} \tilde{\epsilon}^\nu(q, 0) + \frac{q^\mu q^\nu}{m_V^2}. \quad (6)$$

Now, the BRST identities [11,12] for the sub-amplitudes give the corresponding Goldstone boson amplitudes, arriving at the 5×5 representation of the FD gauge propagator

$$P_{\text{FD}}^{MN}(V) = \begin{pmatrix} P_{\text{FD}}^{\mu\nu} & -i\tilde{\epsilon}^\mu(q, 0) \frac{m_V}{Q} \\ i\tilde{\epsilon}^\nu(q, 0) \frac{m_V}{Q} & 1 \end{pmatrix}, \quad (7)$$

where the first 4 components of M and $N = 0, 1, 2, 3$, denoted by μ and ν , respectively, account for the four-vector components of the weak bosons, whereas their fifth components, $M, N = 4$, account for the associated Goldstone boson.²

In refs. [1] and [2], the above FD gauge propagators for the SM gauge bosons, eq. (4) for the photon and gluons and eq. (7) for the W^\pm and Z bosons, have been implemented into the numerical helicity amplitude calculation codes **HELAS** [15,16], and a few modifications were applied to the Feynman rules for some EW vertices [2] such that we can obtain helicity amplitudes of an arbitrary SM processes by using **MadGraph5_aMC@NLO** [17–19] at the tree level. The results presented in refs. [1, 2] are encouraging, since not only all the numerical problems associated with so-called ‘gauge cancellation’ among interfering Feynman amplitudes are absent, but also the helicity amplitudes for individual Feynman diagram seem to have definite physical interpretation, as products of all the invariant Feynman propagator factors for the connecting lines and the splitting amplitudes [3–5] at each vertex. The latter property may allow us to study physics of interference among interfering Feynman amplitudes by using numerical codes.

² The BRST identities between the matrix elements of the operator $\partial^\mu V_\mu(x)$ and those of the Goldstone boson operator $\pi(x)$ at the tree level are ξ independent [13] in the covariant R_ξ gauge [14]. We can take the $\xi \rightarrow \infty$ limit smoothly to obtain the Unitary gauge expression, since all the Goldstone boson couplings are ξ independent.

On the other hand, it has not been made clear how the FD gauge amplitudes are automatically generated for quantum field theory (QFT) models beyond the SM. In addition, it was not clear if the FD gauge propagators can be used in loop calculations, because all what was done in refs. [1, 2] is to replace the known covariant gauge propagators by the FD gauge ones by making use of the BRST identities for the two sub-amplitudes which are connected by a gauge boson line. Because the property that cutting of an internal line gives two sub-amplitudes, each reduces to scattering amplitudes when the cutted line is set on-shell, is a property unique to the tree-level amplitudes, the heuristic derivation given in refs. [1, 2] cannot be applied to loop amplitudes. An alternative approach within the covariant quantization scheme of the electroweak theory has been pursued by the authors of refs. [5, 6].

In this paper, we present an alternative derivation of the FD gauge propagators, in which they are obtained directly as Green’s functions of the equation of motion of the free weak bosons quantized in the Light Cone (LC) gauge. By choosing the LC gauge vector along the opposite of the three-momentum direction of the vector boson [1, 2]

$$n_{\text{FD}}^\mu = (\text{sgn}(q^0), -\vec{q}/|\vec{q}|), \quad (8)$$

we obtain the FD gauge propagators. In this derivation, it is clear that the Goldstone boson degrees of freedom should be the 5th component of the physical weak boson wave functions, and hence no unphysical particles remain in the spectrum, at least in the tree level. The Feynman rules are then obtained straightforwardly in an arbitrary QFT models.

The paper is organized as follows. In section 2, we show how the FD gauge propagator for the weak bosons can be obtained directly from their free equation of motion. In section 3, we show sample results for a few $2 \rightarrow 3$ processes in QED and QCD, comparing Feynman amplitudes in the FD gauge against those in a few generic choices of LC gauges and the Feynman gauge. In section 4, we show our findings for the amplitudes of the process, $\gamma\gamma \rightarrow W^+W^-$ followed by W^\pm decays, where we compare the FD gauge amplitudes against those of a few generic LC gauges and the Unitary gauge. Section 5 summarizes our findings, and outlines how automatic computation in the FD gauge is possible for BSM models, including SM Effective Field Theory (SMEFT).

2 Derivation

The free Lagrangian for the Z boson and the corresponding Goldstone boson (π) in the LC gauge is given by

$$\mathcal{L}^{(0)} = -\frac{1}{4}(\partial^\mu Z^\nu - \partial^\nu Z^\mu)^2 + \frac{1}{2}m^2 Z^\mu Z_\mu + \frac{1}{2}(\partial^\mu \pi)^2 + mZ^\mu \partial_\mu \pi - \frac{1}{2\xi}(n^\mu Z_\mu)^2, \quad (9)$$

where m is the Z boson mass, and ξ and n^μ are the gauge-fixing parameters, satisfying $n \cdot n = 0$. The above La-

grangian can be expressed as

$$\mathcal{L}^{(0)} = \frac{1}{2} \times \begin{pmatrix} Z^\mu & \pi \end{pmatrix} \begin{pmatrix} (\partial^2 + m^2)g_{\mu\nu} - \partial_\mu \partial_\nu - \frac{n_\mu n_\nu}{\xi} & m\partial_\mu \\ -m\partial_\nu & -\partial^2 \end{pmatrix} \begin{pmatrix} Z^\nu \\ \pi \end{pmatrix}, \quad (10)$$

with the 5-component fields (Z^μ, π) , where the derivatives operate to the right-hand side.

The equation of motion (EOM) of the (Z^ν, π) system is then

$$\begin{pmatrix} (\partial^2 + m^2)g_{\mu\nu} - \partial_\mu \partial_\nu - \frac{n_\mu n_\nu}{\xi} & m\partial^\mu \\ -m\partial_\nu & -\partial^2 \end{pmatrix} \begin{pmatrix} Z^\nu(x) \\ \pi(x) \end{pmatrix} = 0. \quad (11)$$

In the momentum space, the EOM reads

$$\begin{pmatrix} (-q^2 + m^2)g_{\mu\nu} + q^\mu q_\nu - \frac{n_\mu n_\nu}{\xi} & -imq^\mu \\ imq_\nu & q^2 \end{pmatrix} \begin{pmatrix} \tilde{Z}^\nu(q) \\ \tilde{\pi}(q) \end{pmatrix} = 0, \quad (12)$$

where $\tilde{Z}^\nu(q)$ and $\tilde{\pi}(q)$ are the Fourier transform of $Z^\nu(x)$ and $\pi(x)$ fields. We can express the EOM (12) as

$$O_N^M \tilde{Z}^N(q) = 0 \quad (13)$$

with $M, N = 0$ to 4, where 0 to 3 are μ, ν , and

$$\tilde{Z}^4(q) = \tilde{Z}_4(q) = \tilde{\pi}(q). \quad (14)$$

The 5×5 matrix O is

$$O_\nu^\mu = (-q^2 + m^2)g_{\mu\nu} + q^\mu q_\nu - \frac{n_\mu n_\nu}{\xi}, \quad (15a)$$

$$O_4^\mu = -imq^\mu, \quad (15b)$$

$$O_\nu^4 = imq_\nu, \quad (15c)$$

$$O_4^4 = q^2. \quad (15d)$$

It is then straightforward to show the following identity:

$$P_M^R O_N^M \tilde{Z}^N(q) = (q^2 - m^2) \delta_N^R \tilde{Z}^N(q) = 0 \quad (16)$$

with the 5×5 matrix

$$P_\mu^\rho = -g_\mu^\rho + \frac{n^\rho q_\mu + q^\rho n_\mu}{n \cdot q} + \xi(q^2 - m^2) \frac{q^\rho q_\mu}{(n \cdot q)^2}, \quad (17a)$$

$$P_4^\rho = i \frac{mn^\rho}{n \cdot q} + i\xi(q^2 - m^2) \frac{mq^\rho}{(n \cdot q)^2}, \quad (17b)$$

$$P_\mu^4 = -i \frac{mn_\mu}{n \cdot q} - i\xi(q^2 - m^2) \frac{mq_\mu}{(n \cdot q)^2}, \quad (17c)$$

$$P_4^4 = 1 + \xi(q^2 - m^2) \frac{m^2}{(n \cdot q)^2}. \quad (17d)$$

The identity (16) tells that all 5-components of $\tilde{Z}^N(q)$ have a common Lorentz invariant mass, satisfying the

equation of motion (12) at an arbitrary Lorentz frame. The LC gauge propagator of the weak boson is then obtained directly as the Green's function of the EOM:

$$G_M^R = \frac{P_M^R}{q^2 - m^2 + i\varepsilon}. \quad (18)$$

It should be noted that the above 5×5 representation of the weak boson propagators were obtained in 1987 by Kunszt and Soper [20] in genral axial gauge. They solve the equation of motion under the constraint,

$$n^\mu V_\mu(x) = 0 \quad (19)$$

for a generic constant four vector n^μ (axial gauge). Our LC gauge Green's function (18) agrees with the one reported in ref. [20] exactly when we set $\xi = n^2 = 0$.

In the following, we set $\xi = 0$ and keep only the light-cone vector n^μ

$$n^\mu = (1, \vec{n}), \quad |\vec{n}| = 1, \quad (20)$$

as the gauge parameter. The 'polarization' tensor in the LC gauge is then

$$P_{LC}^M{}_N = \begin{pmatrix} -g_\nu^\mu + \frac{n^\mu q_\nu + q^\mu n_\nu}{n \cdot q} & im \frac{n^\mu}{n \cdot q} \\ -im \frac{n_\nu}{n \cdot q} & 1 \end{pmatrix}, \quad (21)$$

and the LC gauge propagator is

$$G_{LC}^M{}_N = \frac{P_{LC}^M{}_N}{q^2 - m^2 + i\varepsilon}. \quad (22)$$

The FD gauge propagator is then obtained by setting

$$n^\mu \equiv n_{FD}^\mu = (\text{sgn}(q^0), -\vec{q}/|\vec{q}|) \quad (23)$$

as defined in refs. [1, 2]. By comparing the LC gauge propagator factor (21) with the corresponding FD gauge factor eq. (7), we find

$$\tilde{\varepsilon}^\mu(q, 0) = -\text{sgn}(q^2) \frac{Q n_{FD}^\mu}{n_{FD} \cdot q}, \quad (24)$$

as shown in ref. [2]. It should be noted here that, although the FD gauge propagators can be obtained from the LC gauge propagator (22) simply by choosing the LC gauge vector as (23), the FD gauge is *not* a LC gauge. This is because the FD gauge vector (23) does not transform as a four-vector under the Lorentz transformation, and hence the 'dot product'

$$n_{FD} \cdot q = |q^0| + |\vec{q}| \quad (25)$$

is not Lorentz invariant. It is invariant under rotations while its magnitude transforms as $e^{\pm\eta}$ under boosts with rapidity $\pm\eta$ along the three-momentum direction [2].

We further note that although the LC gauge expression of the 'polarization tensor', eq. (21), has exactly the same form with that of the FD gauge, except for its particular orientation of the gauge vector n^μ , it is only in the FD gauge, the tensor can be expressed in terms of

the polarization vectors with definite helicities, as shown explicitly in eqs. (4) and (7). In general LC gauge, we can also express the polarization tensor in terms of the three polarization vectors as

$$\begin{aligned} P_{LC}^\mu{}_\nu &= -g^\mu{}_\nu + \frac{n^\mu q_\nu + q^\mu n_\nu}{n \cdot q} \\ &= \sum_{\lambda=1,2} \epsilon^\mu(q, \lambda) \epsilon_\nu(q, \lambda)^* \\ &\quad + \text{sgn}(q^2) \epsilon^\mu(q, 3) \epsilon_\nu(q, 3), \end{aligned} \quad (26)$$

where the first two polarization vectors are orthogonal to both q^μ and n^ν ,

$$\sum_{\lambda=1,2} \epsilon^\mu(q, \lambda) \epsilon_\nu(q, \lambda)^* = P_{LC}^\mu{}_\nu - q^2 \frac{n^\mu n_\nu}{(n \cdot q)^2}, \quad (27)$$

and the third one is

$$\epsilon^\mu(q, 3) = \frac{Q n^\mu}{n \cdot q}. \quad (28)$$

However, none of the above three polarization vectors are helicity eigenstates. It is only when the LC gauge vector n^μ is chosen along n_{FD}^μ , the three polarization vectors can be helicity eigenstates.

In the EW theory of the SM, there are triplets of weak bosons, W^1 , W^2 and Z , all of which have the same free Lagrangian as given by eq. (9). The mass term m for W^1 and W^2 is the charged weak boson mass, m_W , and the associated Goldstone boson is π^1 and π^2 , respectively, of the custodial $SU(2)$ triplets. The charge eigenstates, $W^\pm = (W^1 \mp iW^2)/\sqrt{2}$ and $\pi^\pm = (\pi^1 \mp i\pi^2)/\sqrt{2}$ are obtained from the pairs of real fields. Consequently, the 5th component of the charged weak bosons are the Goldstone bosons of the same charge in the LC (and in the FD) gauge.

3 Sample results in QED and QCD

As is clear from the explicit form of the general LC gauge propagators of the SM gauge bosons, the photon, the gluons, and the weak bosons W^\pm and Z , the only difference between the LC gauge and the FD gauge is in the choice of the LC gauge vector n^μ . The Feynman rules to obtain an arbitrary tree-level scattering amplitudes are also identical among all LC gauges, including the FD gauge. This is in particular so, for the $ZZZZ$, $WWZH$ and $WWAH$ vertices which are needed to be introduced in ref. [2], in order to allow **Madgraph** to generate necessary **HELAS** subroutine calls and the corresponding Feynman diagrams.

Since all the **HELAS** numerical codes have been prepared for the FD gauge in refs. [1,2], we introduce a switch in these codes³ which allows us to fix n^μ globally, independent of the gauge boson four momenta. It is only by this minimal modification, the **HELAS** codes prepared for the FD gauge can be used to generate tree-level helicity amplitudes of an arbitrary SM processes.

³ <https://madgraph.ipmu.jp/IPMU/Softwares/HELAS/index.html>

We note in passing that we choose not to introduce the polarization vectors in the generic LC gauge, because they are not helicity eigenstates, as explained in the previous section. When we need to calculate the scattering amplitudes with external on-shell weak bosons, we use the polarization vectors in the FD gauge, so that we can obtain the helicity amplitudes even in the generic LC gauge.

In this section, we show sample results we obtain by using our new programs for simple QED and QCD processes, and also for an EW process in the next section. In all the samples, we compare results of a few LC gauge vector directions against those of the FD gauge and the Feynman gauge (for QED and QCD) and against the Unitary gauge for the EW theory.

3.1 QED

As the first simple example, we study the process

$$e^- + \mu^+ \rightarrow e^- + \mu^+ + \gamma \quad (29)$$

in QED, whose Feynman diagrams are shown in Fig. 1. It should be noted that each Feynman amplitudes of an arbitrary $2 \rightarrow 2$ processes in QED and QCD are gauge invariant among all covariant gauges and in LC gauges, because the photon and the gluon propagators are sandwiched by two conserved currents in both sides.⁴

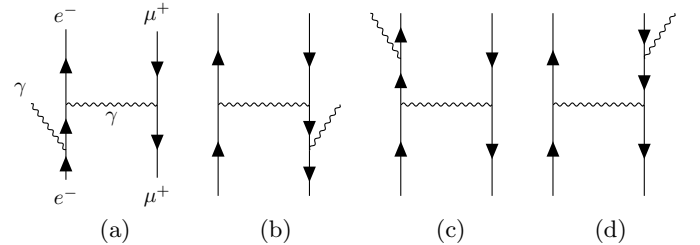


Fig. 1. Feynman diagrams for $e^- \mu^+ \rightarrow e^- \mu^+ \gamma$ in QED⁵.

We also note here that we show $e^- \mu^+$ collision case rather than the $e^+ e^-$ or $\mu^+ \mu^-$ collisions simply to remove $\ell\bar{\ell}$ annihilation contributions. At high energies, at $\sqrt{s} = 250$ GeV and 1 TeV which we study below, the annihilation processes give rise to the so-called radiative return events, where the final lepton pair comes dominantly from the Z boson decays, and the photon is emitted along the beam momentum directions. Although our pure QED amplitudes do not have Z boson contributions, the interference patterns reported in our study may be observable at future $e^+ e^-$ or $\mu^+ \mu^-$ colliders after imposing final state cut like $|m(\ell\bar{\ell}) - m_Z| \gtrsim 15 \Gamma_Z$ to suppress $\ell\bar{\ell}$ annihilation contributions.

⁴ Gauge dependence can appear in general axial gauge due to $n^\mu n^\nu$ term.

⁵ The Feynman diagrams in Figs. 1, 6, and 10 are drawn with **TikZ-FeynHand** [21, 22].

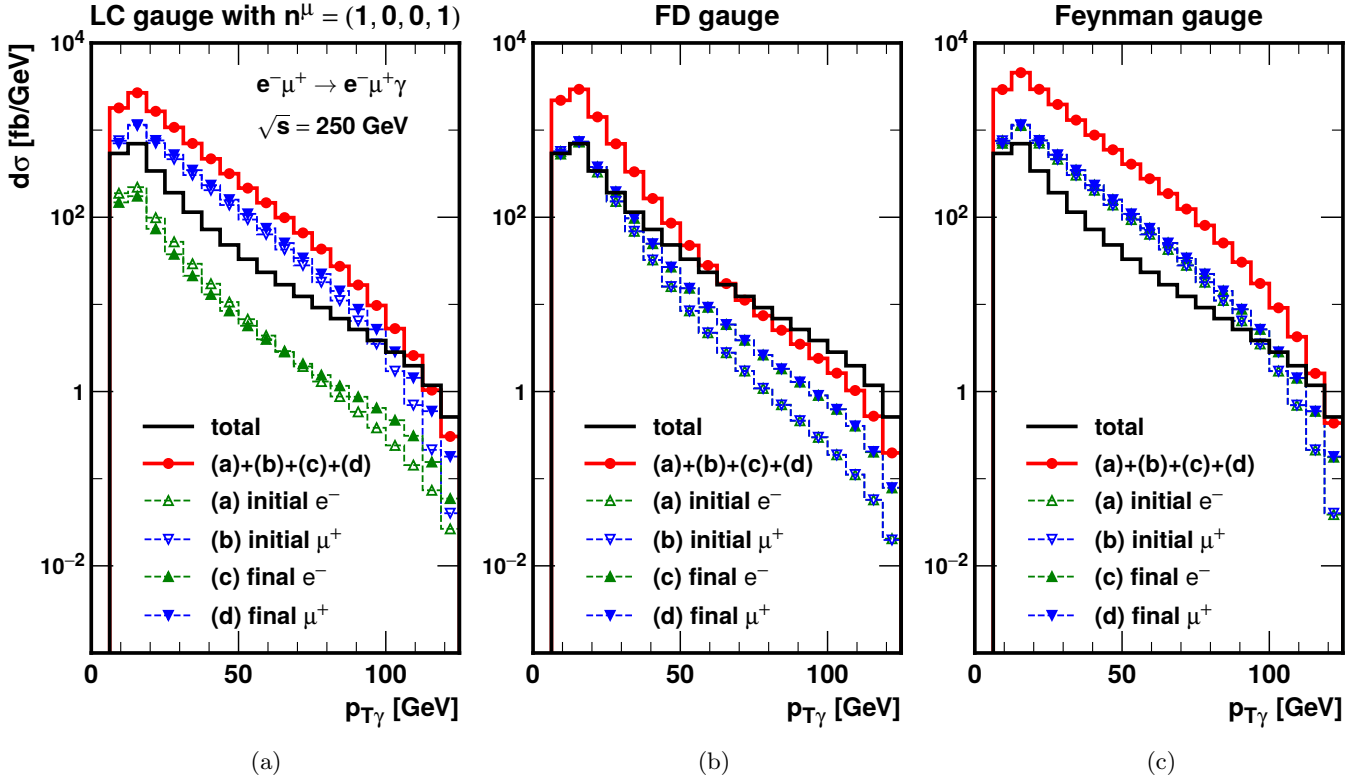


Fig. 2. p_T distributions of the photon for $e^- \mu^+ \rightarrow e^- \mu^+ \gamma$ at $\sqrt{s} = 250$ GeV in different gauges; (a) LC, (b) FD, and (c) Feynman gauges.

We set the minimal kinematical cuts for the final-state particles ($i, j = e, \mu, \gamma$):

$$p_{T_i} > 10 \text{ GeV},$$

$$\Delta R_{ij} = \sqrt{(\eta_i - \eta_j)^2 + (\phi_i - \phi_j)^2} > 0.4. \quad (30)$$

Note that the above final state cuts remove the region of the phase space where the virtuality of the exchanged photon is very small where the Feynman gauge (or in any covariant gauge) amplitudes suffer from serious numerical cancellation among interfering amplitudes [23]. In this paper, we study how the interference patterns among individual Feynman diagram contributions differ among a few selected LC gauges, Feynman gauge, in contrast to the FD gauge.

In Fig. 2, we show the p_T distributions of the photon in the process eq. (29) at $\sqrt{s} = 250$ GeV. We compare three cases, (a) LC gauge with

$$n^\mu = (1, 0, 0, 1), \quad (31)$$

(b) FD, and (c) Feynman gauges. Absolute value square of the four individual Feynman diagram contribution is shown separately, and their sum is given by the solid red histograms. The physical distribution, obtained by summing all the amplitudes before squaring, given by the thick black histograms, are identical (gauge independent) as expected.

We observe from Fig. 2(c) that in the Feynman gauge, the p_T distribution from all the four diagrams are larger

than the physical distribution. Contributions from all the four individual diagrams have similar magnitudes at all p_T range, telling destructive interference among the sub-amplitudes all the way up to $p_T \sim 120$ GeV.

In case of the FD gauge, in Fig. 2(b), we observe that the interference is destructive in the region $p_T \lesssim 60$ GeV, while constructive at $p_T \gtrsim 80$ GeV. The destructive interference for low p_T photon is the property expected for soft-photon radiation, where the γ emitted from the initial $e^- (\mu^+)$ and that from the final $e^- (\mu^+)$ cannot resolve initial and final leptons when the γ p_T is smaller than the final lepton p_T . Indeed, at $p_T \lesssim 30$ GeV, all four diagrams give similar magnitude, and the sum of all four diagrams give essentially the same magnitude with individual contribution, as may be expected for soft photons.

When comparing the above two cases, for the (b) FD gauge and the (c) Feynman gauge, against the Fig. 1(a) for the LC gauge with the LC vector of eq. (31), we notice a striking asymmetry in the individual Feynman diagram contribution between the emissions from the e^- leg (denoted by the histogram with green triangles) and those from the μ^+ leg (denoted by the histograms with blue triangles).

Amplitudes with initial and final state emission from the e^- legs are suppressed, while those from the μ^+ legs are enhanced. Because the sum of the two emission amplitudes, (a) and (c) for the e^- legs, and (b) and (d) for the μ^+ legs, are separately gauge independent, this means that the suppressed (a) and (c) amplitudes interfere construc-

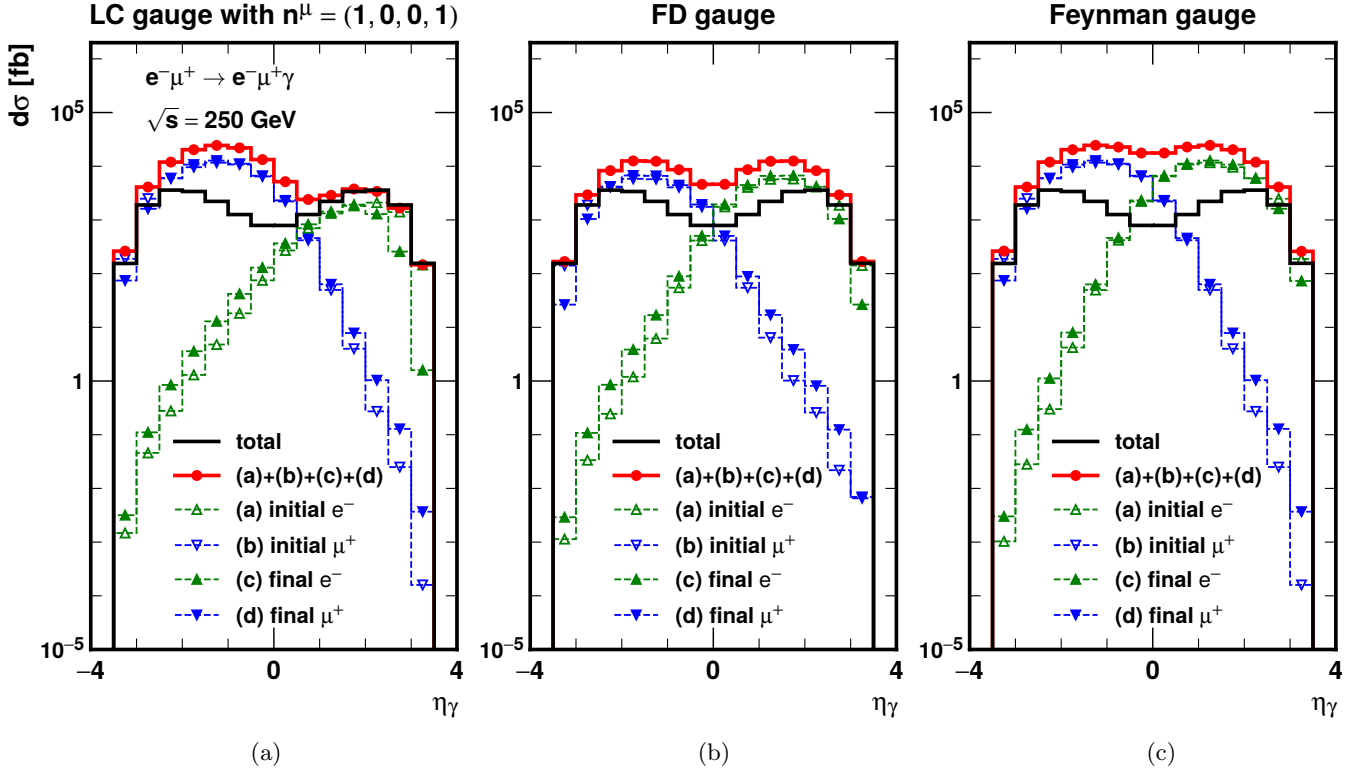


Fig. 3. Same as Fig. 2, but for the photon rapidity η_γ distributions.

tively, and the enhanced (b) and (d) amplitudes interfere destructively, to obtain the same magnitudes.

The reason for the suppression of the amplitudes (a) and (c) can be understood qualitatively as follows. The LC gauge vector (31) is approximately the FD gauge vector for the γ propagators in the diagrams Fig. 1(a) and (c), when the final μ^+ has low p_T satisfying the cut (30), so that the virtual photon momentum is approximately along the initial μ^+ momentum, which is beam energy times $(1, 0, 0, -1)$. These amplitudes are then suppressed because the components which grow with the energy of the virtual gauge bosons are removed by the FD gauge prescription. On the contrary, in diagrams (b) and (d), whose magnitudes are large when the final e^- has low p_T , the LC vector (31) is opposite of the corresponding FD gauge vector, which should be $(1, 0, 0, -1)$ along the virtual γ momentum direction. Rather than subtracting the terms which grow with the energy, these terms are essentially kept untouched to give contributions as big as those in the Feynman gauge, as shown in Fig. 2(c).

Although we do not show results in this report, we examine another choices of the LC gauge vector,

$$n^\mu = (1, 0, 0, -1). \quad (32)$$

As may be expected, the gauge vector (32) reverses the contributions of the photon emissions from the e^- legs, and those from the μ^+ legs. The magnitudes of the amplitudes (a) and (c) are now enhanced, while those of the amplitudes (b) and (d) are suppressed.

In Fig. 3, we show the rapidity (η) distribution of the emitted photon in the process (29) at $\sqrt{s} = 250$ GeV. The

same final state cuts (30) are applied. The FD gauge results in Fig. 3(b) show clearly that the photons emitted from initial and final e^- legs tend to have positive rapidity, while those from initial and final μ^+ legs tend to have negative rapidity, as naively expected from the parton shower behavior. They interfere destructively in the central region, where soft (low p_T) photons from both initial and final emissions can interfere. Similar trends can be observed in the Feynman gauge results shown in Fig. 3(c), but the degree of destructive interference is of the order of $30 \sim 40$ rather than a factor of $5 \sim 7$ in case of the FD gauge.

Finally, the LC gauge results for the gauge vector of eq. (31) is shown in Fig. 3(a). In this plot, we can clearly view the impact of our choice of the gauge vector (31). Even though the amplitudes for the photon emitted from the e^- legs, Fig. 1(a) and (c), are suppressed strongly, they still dominates at very large positive η . We can tell that the diagram Fig. 1(a) for the photon emission from the initial e^- dominates at the highest rapidity region, $\eta \gtrsim 2.5$, while the two diagrams (a) and (c) interfere constructively in the medium positive rapidity region, $1 \lesssim \eta \lesssim 2.5$. Destructive interference between the enhanced amplitudes from the initial and final μ^+ emissions, the Feynman diagrams of Figs. 1(b) and (d), respectively, can be observed at all negative rapidity. The degree of cancellation is as big as in the case of the Feynman gauge, shown in Fig. 3(c).

In Fig. 4, we show results for the process

$$e^- + \mu^- \rightarrow e^- + \mu^- + \gamma \quad (33)$$

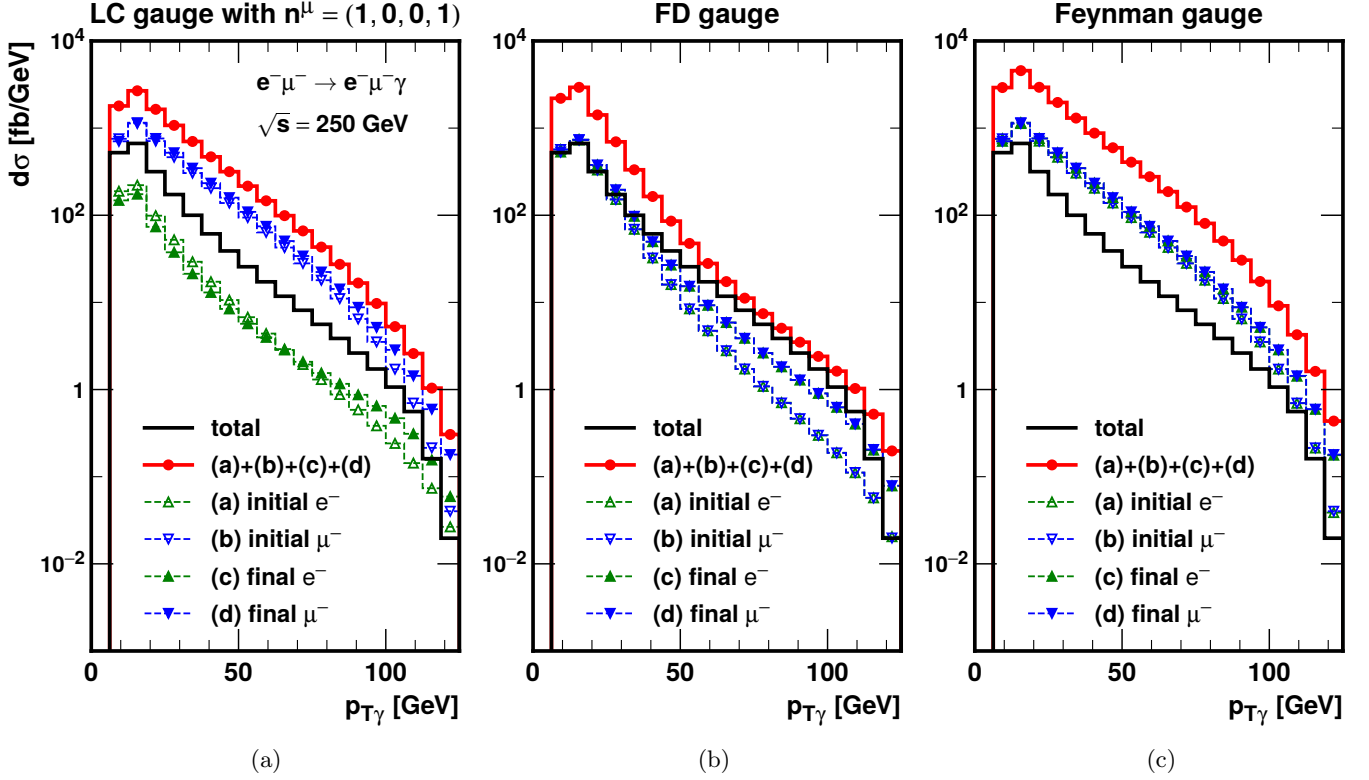


Fig. 4. p_T distributions of the photon for $e^- \mu^- \rightarrow e^- \mu^- \gamma$ at $\sqrt{s} = 250$ GeV in different gauges; (a) LC, (b) FD, and (c) Feynman gauges.

at $\sqrt{s} = 250$ GeV. Here, we want to compare Fig. 2(b) for the $e^- \mu^+$ collisions and Fig. 4(b) for the $e^- \mu^-$ collisions, both in the FD gauge. Because individual Feynman diagram cannot tell the charge of μ^- from that of μ^+ , the absolute value square of each amplitude, and hence their sum, are all the same between Fig. 2 and Fig. 4 for all the gauges. The physically observable distribution, given by the black histogram, is common (gauge independent) among the three gauges shown in Fig. 4, but it is slightly different between Fig. 2 for the process (29) and Fig. 4 for the process (33).

When we compare the two results in the FD gauge, the physical distribution (in thick black histogram) is bigger than the sum of the square of each diagram (given by the thick red histogram) at large p_T , $p_T \gtrsim 70$ GeV, in Fig. 2(b) for the $e^- \mu^+$ collision process (29). On the other hand, in Fig. 4(b) for the $e^- \mu^-$ collision process (33), the physical cross section is never greater than the sum of the square of individual Feynman amplitude at all p_T . Therefore, at large p_T , $p_T \gtrsim 70$ GeV we observe constructive interference among the Feynman amplitudes for the $e^- \mu^+$ collision process (29), whereas destructive interference in case of the $e^- \mu^-$ collision.

This observation is in agreement with what we can expect from the null-radiation zone theorem [24], which tells that the photon emission is absent when the following identity holds

$$\sum_{\text{All charged particles}} Q_j / (p_j \cdot k) = 0, \quad (34)$$

where Q_j and p_j^μ are the charge and four momentum of j^{th} charged particle, and k^μ is the photon four momentum. In ref. [25] the above identity has been applied to the scattering process $ab \rightarrow cd\gamma$ and the following conditions are obtained:

$$Q_a = Q_b = Q_c = Q_d, \quad (35a)$$

$$\eta(\gamma) = \eta(a + b) = 0, \quad (35b)$$

$$p_T(c) = p_T(d), \quad (35c)$$

in the $a + b$ collision c.m. frame. Here, $\eta(\gamma) = \eta_\gamma$ and $\eta(a + b)$ are the rapidity of the photon and the colliding $a + b$ system. The theorem tells that in the c.m. frame of the $e^- \mu^-$ collision process (33), there should be a perfect destructive interference among the amplitudes when the final e^- and μ^- have the same p_T and the rapidity of the photon is zero. We can observe that these conditions are relatively easy to be satisfied when the photon p_T is large, because large p_T photons tend to have small rapidity, and the recoil particles e^- and μ^- tend to have p_T of the same order of magnitude.

The destructive interference associated with the presence of the null radiation zone at high photon p_T for the $e^- \mu^-$ collision process (33) implies that strong constructive interference should be expected for the $e^- \mu^+$ collision process (29) at the same kinematical configuration [25, 26]. When individual Feynman amplitudes are expressed in the FD gauge, this physical picture can be manifestly observed, as shown by the high p_T behavior

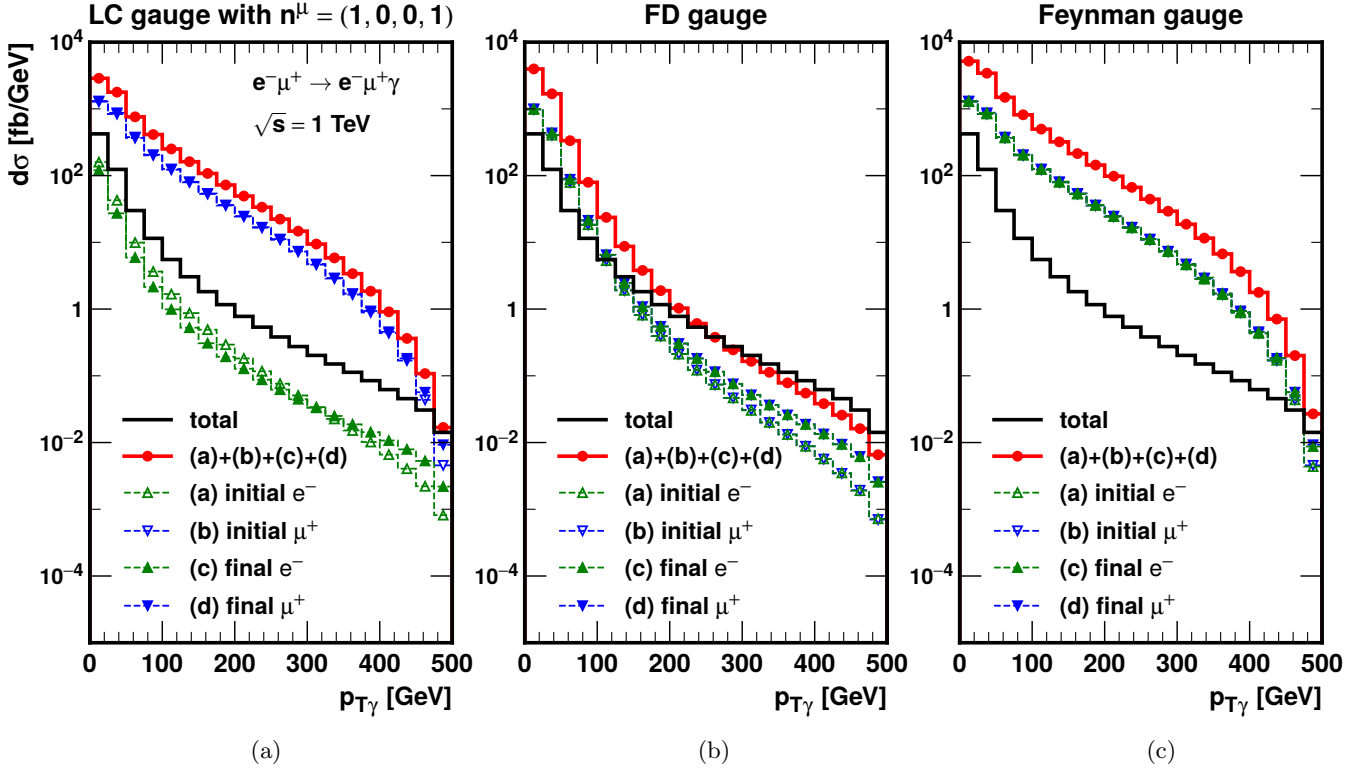


Fig. 5. p_T distributions of the photon for $e^- \mu^+ \rightarrow e^- \mu^+ \gamma$ at $\sqrt{s} = 1$ TeV in different gauges; (a) LC, (b) FD, and (c) Feynman gauges.

shown in Figs. 2(b) and 4(b). Since the null radiation theorem accounts only for classical charged currents, both the destructive and constructive interference patterns are independent of the lepton helicities.

In contrast, individual Feynman amplitudes are not enlightening in studying such interference patterns, as can be observed by comparing Figs. 2(c) and 4(c) for the Feynman gauge, and by comparing Fig. 2(a) and 4(a) for the LC gauge.

Although we study only the interference patterns for soft-photon emissions and those associated with the null radiation theorem in this report, the FD gauge amplitudes may tell us more about physics of interference among Feynman amplitudes.

Before closing the subsection on the QED amplitudes, let us show in Fig. 5 the photon p_T distribution of the process (29) $e^- \mu^+ \rightarrow e^- \mu^+ \gamma$ at $\sqrt{s} = 1$ TeV. As in Fig. 2, the three figures are for (a) LC gauge with $n^\mu = (1, 0, 0, 1)$, (b) FD gauge, and (c) Feynman gauge.

The destructive interference at low p_T , as expected for soft photon, and the constructive interference at high p_T , consistent with prediction of the classical radiation zero theorem [24], are clearly seen in the FD gauge, in Fig. 5(b). Although both LC gauge and Feynman gauge results don't give us such insights, we can tell by comparing Fig. 5(a) and (c) that the magnitude of physical enhancement of the amplitudes which are not suppressed by the LC gauge vector of $n^\mu = (1, 0, 0, 1)$, Figs. 1(b) and (d), are as large as those of the Feynman gauge. The difference is that in

case of the Feynman gauge, Fig. 5(c), all four amplitude squares are large, and hence their sum given by the red histogram is about twice as large as the corresponding sum in Fig. 5(a) for the LC gauge.

3.2 QCD

In this subsection, we study LC gauge amplitudes in QCD $2 \rightarrow 3$ processes, and compare with the FD gauge and the Feynman gauge predictions [1]. For the quark-quark scattering process $ud \rightarrow udg$ [1], we find that it gives more or less similar results to the QED example of $e^- \mu^\pm \rightarrow e^- \mu^\pm \gamma$ shown in the previous subsection. Therefore, we only present our studies on the process

$$g(p_1) + g(p_2) \rightarrow g(p_3) + g(p_4) + g(p_5). \quad (36)$$

The Feynman diagrams are depicted in Fig. 6, where we omit six diagrams with the four-point vertex in the column (e). The diagrams are grouped into 5 types along columns. In the first column, type (a), the gluon (5) is emitted from $g(1)$. Likewise, $g(5)$ is emitted from $g(2)$ in the second column (b), a virtual gluon splits into $g(3)$ and $g(5)$ in (c), or into $g(4)$ and $g(5)$ in (d). In the diagrams of type (e), $g(5)$ is emitted from an exchanged virtual gluon or from the four-point vertex.

Event samples of $gg \rightarrow ggg$ are generated for pp collisions at $\sqrt{s} = 13$ TeV, by using the gluon PDF of ref. [27]. We impose the following final state cuts:

$$p_{Ti} > 20 \text{ GeV}, \quad (37a)$$

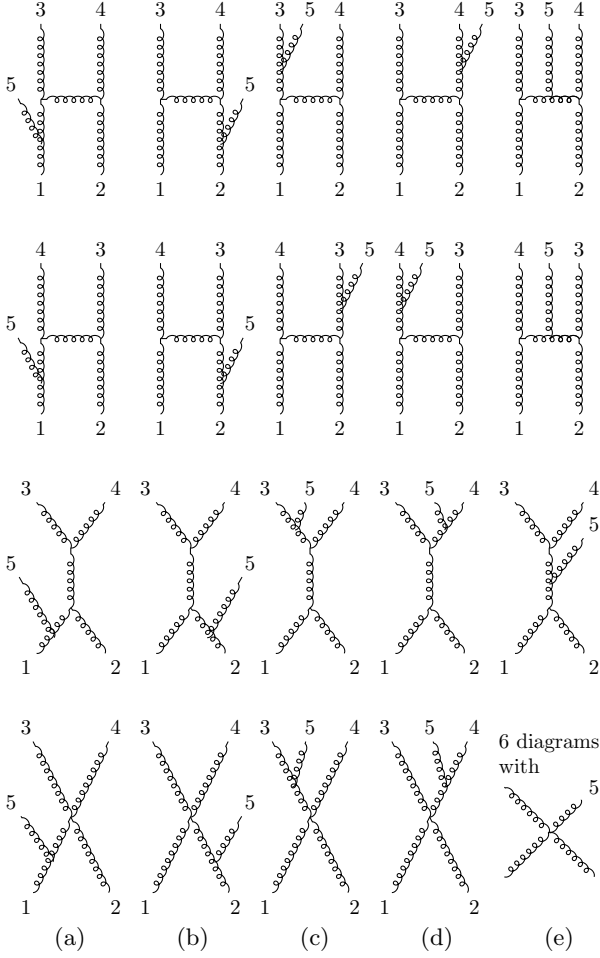


Fig. 6. Feynman diagrams for $gg \rightarrow ggg$.

$$|\eta_i| < 4.5, \quad (37b)$$

$$\Delta R_{ij} = \sqrt{(\eta_i - \eta_j)^2 + (\phi_i - \phi_j)^2} > 0.4, \quad (37c)$$

for $i, j = 3, 4, 5$ for the final state gluons in eq. (36). We set the scale of the colliding gluon PDF at $Q = 200$ GeV, and fix the QCD coupling at $\alpha_S = \alpha_S(200 \text{ GeV}) = 0.106$.

The initial gluon $g(p_1)$ has momentum along the positive z -axis, while $g(p_2)$ momentum is along the negative z -axis. The three final state gluons are identified by p_T ordering,

$$p_{T3} > p_{T4} > p_{T5}, \quad (38)$$

and we introduce a hard scale of two high p_T jet production by requiring

$$p_{T3}, p_{T4} > 200 \text{ GeV}. \quad (39)$$

With the above setups, we can study the soft gluon radiation patterns by the p_5 dependences of the lowest p_T jet.

Thanks to the selection cut of (39), we can interpret the 5 groups of the Feynman diagrams in Fig. 6 representing the 5 types of parton shower histories: the 4 diagrams in the column (a) contribute to initial state radiation from

$g(1)$ before the hard $2 \rightarrow 2$ scattering process, the 4 diagrams in the column (b) contribute to initial state radiation from $g(2)$, while those in the column (c) contribute to the final state radiation from the hard jet $g(3)$, those in the column (d) contribute to the final state radiation from the hard jet $g(4)$, whereas the 9 diagrams in the column (e) contribute to soft gluon $g(5)$ emission from the hard $2 \rightarrow 2$ scattering process as a whole.

In Fig. 7, we show the boost invariant distribution of the rapidity difference

$$\eta_5 - \eta_{34}, \quad (40)$$

where η_{34} denotes the rapidity of the hard scattering object, the system of $g(3)$ and $g(4)$, whose four momentum is $p_3 + p_4$. We show the results obtained in three different gauges, in (a) LC gauge with $n^\mu = (1, 0, 0, 1)$, (b) FD gauge, and (c) Feynman gauge.

There are 25 Feynman diagrams for the process $gg \rightarrow ggg$ as depicted in Fig. 6. The physical cross section depends on the squared of the sum of all the 25 Feynman amplitudes,

$$\left| \sum_{k=1}^{25} \mathcal{M}_k \right|^2, \quad (41)$$

which are given by solid black histograms. As expected, they agree exactly among the three gauges. What we show by solid red histograms are the contribution of

$$\sum_{k=1}^{25} |\mathcal{M}_k|^2, \quad (42)$$

that is, the sum of the absolute value squares of all 25 individual Feynman amplitudes. Where the red histogram is significantly above the black histogram, we can tell that subtle cancellation among Feynman amplitudes takes place. Furthermore, contribution to the red histograms are divided into 5 groups, denoted by (a) to (e), according to those in the 5 columns, respectively, in Fig. 6.

As expected, we find that there is no subtle gauge theory cancellation in the FD gauge, as shown in Fig. 7(b), where the red-solid histogram is almost degenerate with the observable black-solid histogram in most region of the rapidity difference, $|\eta_5 - \eta_{34}| \lesssim 8$. The large positive region of the rapidity difference is dominated by the initial state radiation from $g(1)$, the diagram group (a), whereas the large negative region is dominated by the initial state radiation from $g(2)$, the diagram group (b). The central region is populated by gluon emission from the final state hard gluons, $g(3)$ or $g(4)$. Soft gluon emission from the hard process, depicted by orange histogram, populates in the central region but is always subdominant.

In comparison, in both the LC gauge and in the Feynman gauge, the red solid histogram is significantly above the black solid histogram in a broad region of the rapidity difference. The contributions from initial state radiations, the Feynman diagram groups (a) and (b) in Fig. 6 dominate the Feynman gauge distribution in Fig. 7(c), while in Fig. 7(a) for LC gauge with $n^\mu = (1, 0, 0, 1)$, only the initial state radiation from $g(1)$ gets large.

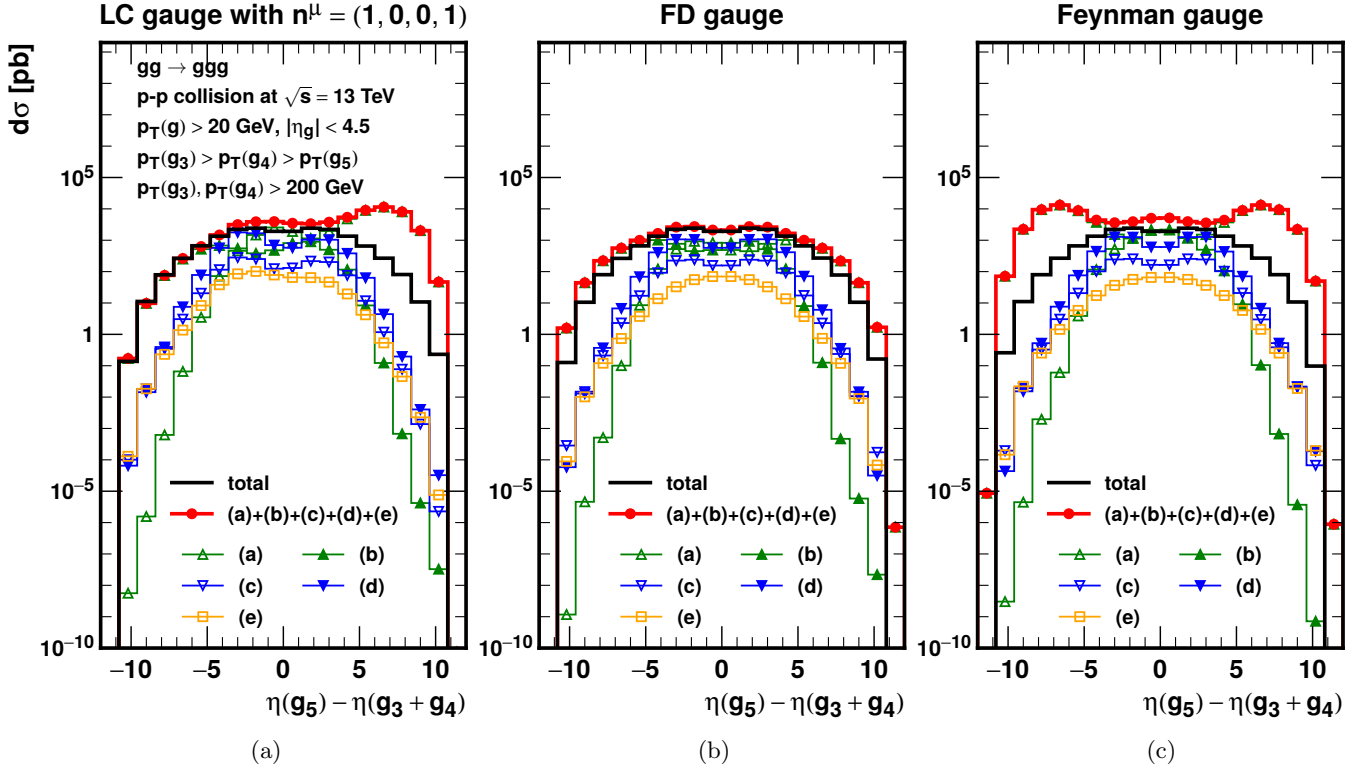


Fig. 7. Distributions of the rapidity difference, $\eta_5 - \eta_{34}$, where η_{34} is the rapidity of the hard di-jet system of two gluons, $g(p_3)$ and $g(p_4)$, in $gg \rightarrow ggg$ subprocess contribution to pp collisions at $\sqrt{s} = 13$ TeV. They are calculated in (a) LC gauge with $n^\mu = (1, 0, 0, 1)$, (b) FD gauge, and (c) Feynman gauge. The black solid histogram gives the cross section predicted by QCD, and hence agrees among the three plots, while the red solid histogram shows the sum of the absolute value square of each Feynman amplitude. Sub-contributions from the 5 groups of Feynman diagrams in Fig. 6 are also shown.

Cross examination of the three plots in Fig. 7 reveals the followings. The degree of cancellation, or the ratio of the red and black histograms grow sharply at $\eta_5 - \eta_{34} \gtrsim 4$ both in the LC gauge, Fig. 7(a), and in the Feynman gauge, Fig. 7(c). Although the red histogram is symmetric about $\eta_5 - \eta_{34} = 0$ in both FD and Feynman gauges, we observe no significant cancellation in the region of $\eta_5 - \eta_{34} < -4$ in case of the LC gauge with $n^\mu = (1, 0, 0, 1)$, where the red and black histograms are almost degenerate. Looking back to the FD gauge results shown in Fig. 7(b), we notice that there is a signal of non-negligible destructive interference at very large rapidity difference, $|\eta_5 - \eta_{34}| \gtrsim 8$. If the FD gauge amplitudes are physical, the destructive interference observed in Fig. 7(b) at large $|\eta_5 - \eta_{34}|$ should have physical interpretation, whereas the absence of cancellation at $\eta_5 - \eta_{34} < -8$ in Fig. 7(a) should be a gauge artefact, or a specifically arranged benefit [9, 10], of the particular LC gauge vector. We will come back to this problem below, after studying the di-jet invariant mass distribution.

In Fig. 8, we show the distribution of the minimum of the three di-jet masses in the final state,

$$\min(m_{ij}) = \min\{m_{34}, m_{35}, m_{45}\}, \quad (43)$$

where m_{ij} denotes the invariant mass of the final $g(p_i)$ and $g(p_j)$ system. The three gauge cases are shown again

for the LC gauge with $n^\mu = (1, 0, 0, 1)$ in Fig. 8(a), the FD gauge in Fig. 8(b), and the Feynman gauge in Fig. 8(c).

As expected, the red histogram is almost degenerate with the black histogram in Fig. 8(b) for the FD gauge, up to $\min(m_{ij}) \simeq 350$ GeV, which confirms that there is no significant cancellation in the FD gauge at small $\min(m_{ij})$. At smallest mass region, the contribution of the diagrams in (d), final state emission from $g(4)$ dominates, the contributions from the initial state radiations, the diagrams (a) and (b) are sub-dominant, followed by the final state emission from $g(3)$. Soft radiation contribution from the group (e) is small at all mass range.

In contrast, the red histogram increases with the di-jet mass up to ~ 500 GeV in case of the Feynman gauge in Fig. 8(c), whereas in case of the LC gauge with $n^\mu = (1, 0, 0, 1)$ in Fig. 8(a), the red histogram stays about constant up to ~ 500 GeV. In case of the Feynman gauge, the large unphysical contribution is dominated by the two initial state radiation contributions, the diagram groups (a) from $g(1)$ and those (b) from $g(2)$. Their contributions, depicted by green triangles and by green up-side down triangles, respectively, are identical. On the other hand, in the LC gauge with $n^\mu = (1, 0, 0, 1)$, the contribution from the initial radiation from $g(2)$, depicted by green up-side-down triangles, is suppressed. The huge unphysical contribution at large mass region is hence dominated by initial state radiation from $g(1)$, denoted by green trian-

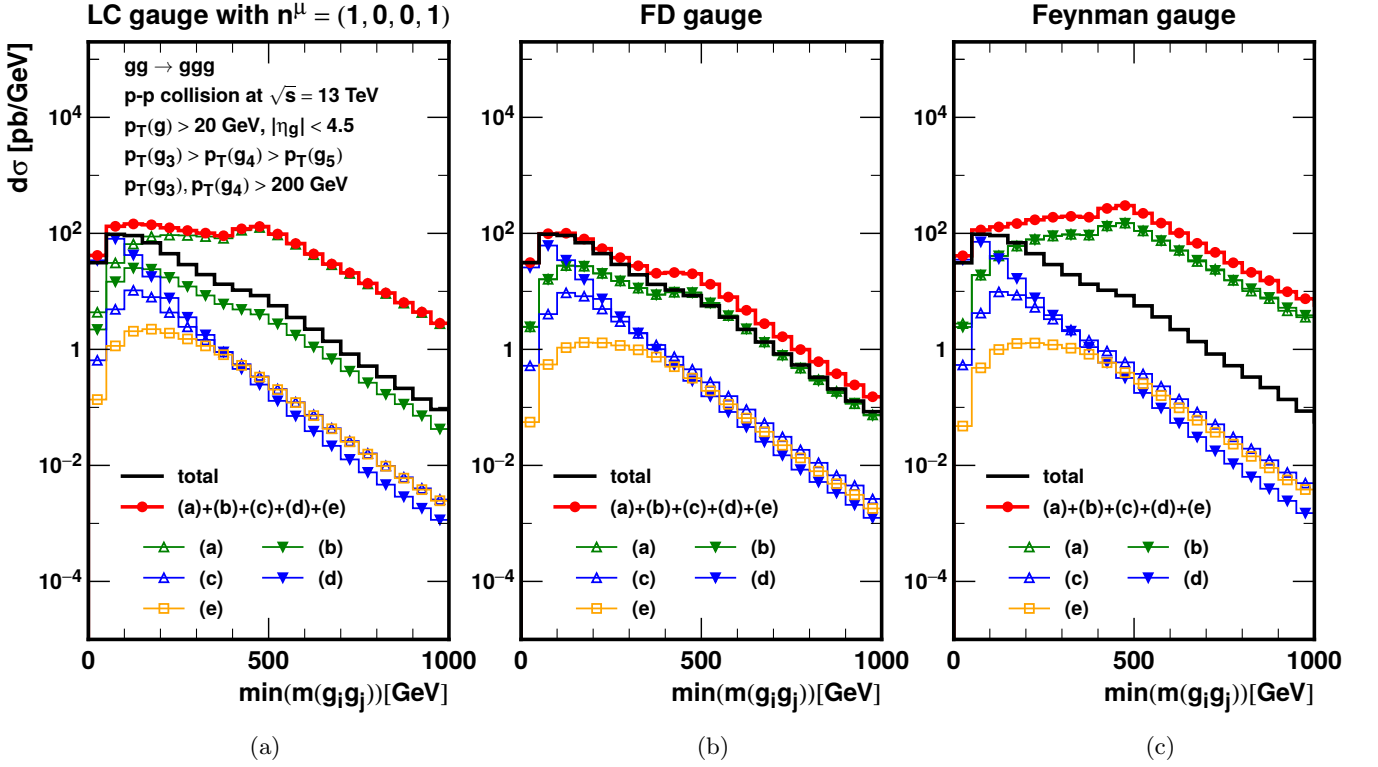


Fig. 8. The same as Fig. 7, but for the distribution of $\min(m_{ij})$, where m_{ij} are the invariant mass of the final state di-gluons among $g(p_3)$, $g(p_4)$ and $g(p_5)$.

gles. As in our QED studies, this shows that the virtual gluon propagator in the initial state radiation diagrams in the column (b) in Fig. 6, is suppressed for $n^\mu = (1, 0, 0, 1)$, because it is collinear to the FD gauge vector for the same propagator when emitted gluon $g(5)$ is soft. The role of the initial state radiation from $g(1)$ and $g(2)$ is interchanged if we choose the LC gauge vector as $n^\mu = (1, 0, 0, -1)$.

In all gauges, the smallest mass region is dominated by the final state emission amplitudes, those of the group (d), as expected. The unphysical gauge cancellation becomes significant above the invariant mass around 200 GeV both for the (a) LC gauge, and for the (c) Feynman gauge.

Let us now examine the distinct behavior of the red histogram around the medium di-jet mass region in Fig. 8(b) for the FD gauge. The red histogram stays almost constant for the three bins, in the range

$$350 \text{ GeV} \lesssim \min(m_{ij}) \lesssim 500 \text{ GeV} \quad (44)$$

In addition, significant destructive interference is observed in the region $\min(m_{ij}) \gtrsim 400 \text{ GeV}$. If the FD gauge amplitudes are all physical, we will be able to identify the cause of the peculiar behavior of the red histogram. We can also find the origin of the destructive interference which makes the black histogram smooth.

We first note that the kink of the red histogram at $\min(m_{ij}) \simeq 400 \text{ GeV}$ is observed in all gauges, which is dominated by the diagrams with initial state radiations, (a) and/or (b). Since non-analytic behavior of the cross sections can only appear through our kinematical cuts, as depicted by eqs. (37) and (39), we examine the 3-jet

configuration which is constrained by the cuts. We find that the region around

$$\min(m_{ij}) \simeq 350 \text{ GeV} \quad (45)$$

is dominated by the events where

$$\eta_3 \simeq \eta_4 \simeq \pm 4.5. \quad (46)$$

That is, both hard jets with $p_T > 200 \text{ GeV}$, eq. (39), are at the boundary of our rapidity cuts, eq. (37b). The soft gluon $g(5)$ satisfying $p_T > 20 \text{ GeV}$, eq. (37a), can combine with either $g(3)$ or $g(4)$ to make $\min(m_{ij})$, while satisfying the jet separation cut of (37c). For instance, in the positive rapidity region, the kinematical configuration of

$$p_3^\mu = 220 \text{ GeV}(\cosh 4.5, 1, 0, \sinh 4.5), \quad (47a)$$

$$p_4^\mu = 200 \text{ GeV}(\cosh 4.5, -1, 0, \sinh 4.5), \quad (47b)$$

$$p_5^\mu = 20 \text{ GeV}(\cosh 4.1, -1, 0, \sinh 4.1), \quad (47c)$$

satisfies the p_T balance and all the selection cuts of eqs. (37)-(39). We find

$$\min(m_{ij}) = m_{45} \simeq 333 \text{ GeV}. \quad (48)$$

When $g(5)$ has azimuthal angles and rapidities satisfying the separation conditions of eq. (37c), the minimum di-jet mass stays in the region of $350 \text{ GeV} \lesssim \min(m_{ij}) \lesssim 500 \text{ GeV}$ where we observe a plateau in the red histogram of Fig. 8(b). Most importantly, the rapidity of the two hard jets, $g(3)$ and $g(4)$, stay around their edge values of ± 4.5 allowed by our event selection cut (37b).

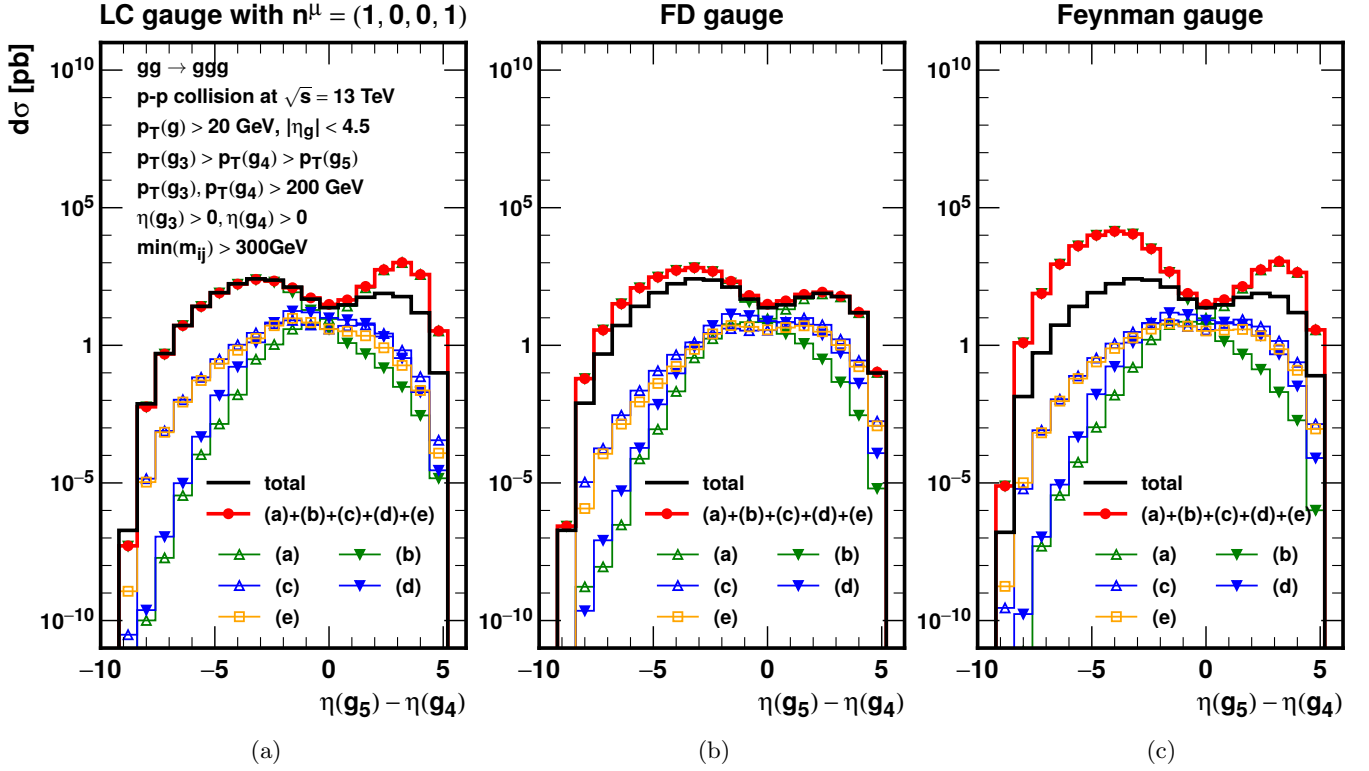


Fig. 9. The same as Fig. 7 but for distributions of the rapidity difference $\eta_5 - \eta_4$, in $gg \rightarrow ggg$ subprocess contribution to pp collisions at $\sqrt{s}=13$ TeV when $\min(m_{ij}) > 300$ GeV and $\eta_3, \eta_4 > 0$.

We now understand the cause of the destructive interference as observed in the region of (44) as in Fig. 8(b). The soft gluon $g(5)$ cannot have larger rapidity than the hard jets, $g(3)$ and $g(4)$, because their rapidities are at the maximum value accepted by our selection cuts. Almost all $g(5)$ rapidity should hence satisfy

$$\eta_5 < \eta_3, \eta_4, \quad (49)$$

in the positive rapidity region, and hence the soft gluon is emitted with larger polar angle than the hard jets. The destructive interference we observe in Fig. 8(b) should hence be due to the same physics mechanism that leads to the angular ordering [28–30] of QCD jet evolutions.

As a confirmation of our observation, we show in Fig. 9 the distribution of the rapidity difference

$$\eta_5 - \eta_4 \quad (50)$$

for those events which satisfy

$$\min(m_{ij}) > 300 \text{ GeV} \quad (51)$$

and for the hemisphere of $\eta_3, \eta_4 > 0$. The destructive interference in the region of $\eta_5 - \eta_4 < 0$ is clearly seen by comparing the red and black histograms in Fig. 9(b) for the FD gauge. We observe no significant interference in the region of $\eta_5 - \eta_4 > 0$, where the soft gluon $g(5)$ has smaller polar angle than the hard jet.

We note that this cancellation of large angle soft gluon emission is what we observe in the inclusive rapidity difference distribution in Fig. 7(b) in the region of large $|\eta_5 - \eta_{34}|$. The destructive interference effect is enhanced in Fig. 9(b)

because we select those events with $\min(m_{ij}) > 300$ GeV in eq. (51), where the effect is found to be large in the di-jet mass distribution of Fig. 8(b).

In contrast to the FD gauge case we study above, the Feynman gauge results in Fig. 9(c) show that significant destructive interference is found both in the positive and negative rapidity ordering, whereas the LC gauge results for $n^\mu = (1, 0, 0, 1)$ in Fig. 9(a) show strong destructive interference at $\eta_5 > \eta_4$ but no significant interference effects at $\eta_5 < \eta_4$. Although detailed study of the LC gauge vector dependence of the gluon emission patterns in QCD amplitudes are beyond the scope of this report, we note here that the vector $n^\mu = (1, 0, 0, 1)$ is along the opposite momentum direction of the initial gluon $g(2)$, which is regarded as a parent of the gluons emitted in the negative rapidity region. Likewise, if we choose the LC vector as $n^\mu = (1, 0, 0, -1)$, the subtle gauge theory cancellation observed in the region of large positive rapidity difference in Figs. 7(a) and 9(a) disappears, and re-appears in the negative rapidity difference regions. Therefore, if we choose $n^\mu = (1, 0, 0, 1)$ for those events with $\eta_5 - \eta_{34} > 0$, while $n^\mu = (1, 0, 0, -1)$ for events with $\eta_5 - \eta_{34} < 0$, we can obtain the exact QCD matrix elements with almost no cancellation for the $gg \rightarrow ggg$ subprocess.

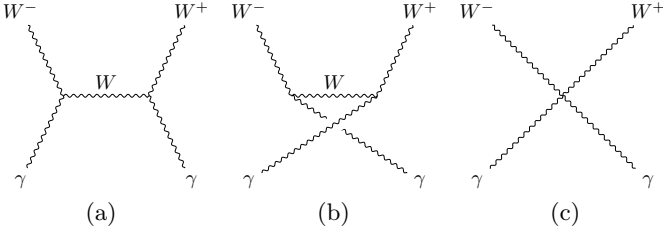


Fig. 10. Feynman diagrams for $\gamma\gamma \rightarrow W^-W^+$.

4 Studies in an EW process

In this section, we study an EW process

$$\gamma + \gamma \rightarrow W^- + W^+. \quad (52)$$

There are three Feynman diagrams for the process, as shown in Figs. 10(a), (b), (c), corresponding to t - and u -channel W exchange, and the contact term, respectively. We study the cross section for the process with both W bosons decay into massless fermion pair, in order to avoid introducing the weak boson polarization vectors in general LC gauge, which are not helicity eigenstates. Specifically, we examine leptonic decays,

$$W^- \rightarrow e^- \bar{\nu}_e, \quad W^+ \rightarrow \mu^+ \nu_\mu. \quad (53)$$

Once W^\pm decays, we will have three weak boson propagators in the diagrams (a) and (b), and two weak boson propagators in the diagram (c).

In the LC gauge, we assign the same LC gauge vector n^μ for all the W^\pm propagators. In this report, we examine the following three gauge vectors:

$$n^\mu = (1, 0, 0, 1) \quad (54a)$$

$$n^\mu = (1, 1, 0, 0) \quad (54b)$$

$$n^\mu = (1, \vec{p}_{W^-} / |\vec{p}_{W^-}|) \quad (54c)$$

The first choice (54a), is the same as eq. (31) employed in previous QED and QCD studies. The second choice (54b) specifies the scattering plane of the process, which takes place in the (x, z) plane. The third gauge vector (54c) is chosen along the W^- momentum direction, opposite to the W^+ momentum direction.

In Fig. 11, we show the differential cross section with respect to $\cos \theta_{W^-}$ in the $\gamma\gamma$ collision rest frame. Here θ_{W^-} is the scattering angle of W^- , or that of e^- and $\bar{\nu}_e$ pair, measured from one of the incoming photon momentum direction. The energy is set high at $\sqrt{s} = 2$ TeV, in order to demonstrate that the LC gauge amplitudes for the weak boson scattering processes are free from the terms which grow with the weak boson energy, as observed already in 1987 by Kunszt and Soper [20], by Dams and Kleiss in 2004 [31] and more recently for the process $\gamma\gamma \rightarrow W^+W^-$ by Bailey and Harland-Lang [32] ⁶

⁶ The authors of refs. [20, 31, 32] adopt general axial gauge, while we can regard our LC gauge as a special case of the axial gauge.

The cross section is obtained by integrating out the invariant masses of the final lepton pairs in the range

$$|m(e^- \bar{\nu}_e) - m_W|, |m(\mu^+ \nu_\mu) - m_W| < 15 \Gamma_W \quad (55)$$

for $m_W = 80.4$ GeV and $\Gamma_W = 2.1$ GeV [33]. Numerical results are obtained for the EW couplings $\alpha = \alpha(m_Z) = 1/128$ and $\sin^2 \theta_W = 0.231$.

The Unitary gauge results as displayed in Fig. 11(c) show clearly the $(E_W/m_W)^2$ growth of the individual Feynman amplitude, where the amplitude with the contact interaction diagram, Fig. 10(c), illustrated by the red dashed curve dominates at all $\cos \theta_{W^-}$. All three amplitudes are large at around $\cos \theta_{W^-} = 0$, where the cancellation makes the physical cross section more than three orders of magnitude smaller than the square of the individual amplitudes. This has been well known, since even the conserved current of massless lepton pair has longitudinal polarization component, which grows with energy in the Unitary gauge. In fact, when massless lepton currents are attached to the weak bosons, whether in the initial state or in the final state of the weak boson scattering processes, there is no gauge dependence in the weak boson propagators within the covariant R_ξ gauge, since the current is conserved (no terms with $q^\mu q^\nu$ survive) and it has no Goldstone boson coupling in the massless limit. The huge growth of the individual amplitude at high energies, as shown in Fig. 11(c), is common to all the covariant R_ξ gauges.

On the contrary, in Figs. 11(a) and (b), there is no subtle cancellation among the three amplitudes in the LC gauge with the gauge vector (54a) and in the FD gauge. We note that in both gauges, single diagram dominates the full amplitude at $|\cos \theta_{W^-}| \approx 1$. In particular, the t -channel exchange amplitude Fig. 10(a) dominates the forward region $\cos \theta_{W^-} \gtrsim 0.6$, while the u -channel exchange amplitude dominates the backward region $\cos \theta_{W^-} \lesssim -0.6$. This has been expected for the FD gauge, as it is designed to make individual Feynman amplitude behave as products of the Feynman propagator factors connected by the physical splitting amplitude at each vertex. The LC gauge results with the gauge vector (54a) are very similar to the FD gauge. It can be understood as follows. In the limit of $|\cos \theta_{W^-}| = 1$, the t - and u -channel exchange weak boson three momenta are either along the positive or the negative z -axis. In this limit, where the cross section is the largest, the LC gauge vector agrees with the FD gauge vector, up to the sign of the three-vector piece. This sign dependence does not affect the amplitudes in the process (52) because the amplitude is symmetric in the exchange of two incoming photons.

On the other hand, the Unitary gauge results show that even near the $|\cos \theta_{W^-}| = 1$ limits, the distribution behavior is unusual. The t -channel exchange amplitude, whose absolute square is given by the blue curve in Fig. 11(c), decreases with $\cos \theta_{W^-}$, quite opposite of what we naively expect from the Feynman's propagator behavior. Then at the last $\cos \theta_{W^-}$ bin of the histogram, $0.95 < \cos \theta_{W^-} < 1$, the t -channel exchange amplitude dominates the physical amplitude, and the other two amplitudes with larger magnitudes cancel out almost exactly.

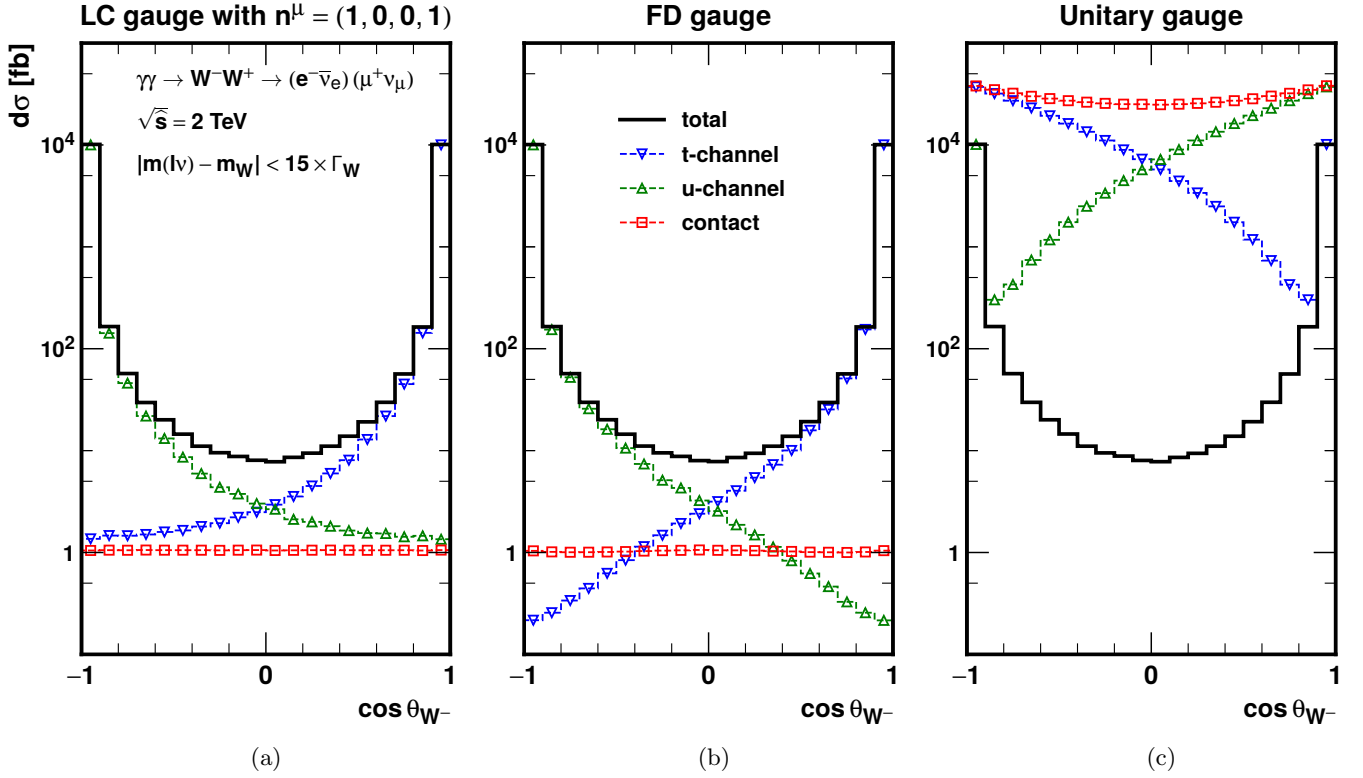


Fig. 11. Distribution of the scattering angle for $\gamma\gamma \rightarrow W^-W^+$ at $\sqrt{s} = 2$ TeV in three different gauges: (a) LC gauge with $n^\mu = (1, 0, 0, 1)$, (b) FD gauge, and (c) the Unitary gauge. The invariant masses of the final lepton pairs are integrated out in the W resonant region, $|m(e^-\bar{\nu}_e) - m_W|, |m(\mu^+\nu_\mu) - m_W| < 15 \Gamma_W$.

Although we do not look into more details on this, it is clear that the Unitary gauge, or any other covariant R_ξ gauge amplitudes are often impractical in obtaining physical insights out of individual scattering amplitudes.

Next, we study the LC gauge results with other gauge vectors, eqs. (54b) and (54c). We find unexpectedly that our Monte Carlo integration program doesn't produce results for these two gauge vectors. Although the problem associated with the LC gauge singularity may have been well known [34], we would like to share in this report what we learn by using our new automatic amplitude calculation code.

We first note that all the LC gauge amplitudes give exactly the same cross section when both W 's are on the mass-shell:

$$m(e^-\bar{\nu}_e) = m(\mu^+\nu_\mu) = m_W. \quad (56)$$

The three plots of Fig. 12 show the differential cross section with respect to $\cos\theta_{W^-}$ when the final state is constrained to satisfy the double on-shell conditions (56). The black solid histograms are obtained from the physical amplitudes where the three Feynman diagrams of Fig. 10 are summed before squaring. The gauge invariance of the physical amplitudes are clearly observed from the exact agreement of the three black histograms in Fig. 12. The individual Feynman diagram contributions, however, are very different among the three LC gauges. The gauge vector (54a) gives distributions which are consistent with the behavior of the corresponding Feynman propagator in the

t - and u -channels, and its absence in the contact term, just as in the FD gauge. For the gauge vector (54b), each Feynman amplitude gives approximately the same magnitude at $|\cos\theta_{W^-}| \gtrsim 0.6$ as that of the LC gauge (54a). All the three Feynman amplitudes, however, have large magnitude at around $\cos\theta_{W^-} \approx 0$, where destructive interference among the three amplitudes give the physical cross section. In case of the gauge vector (54c), the enhancement of the magnitude of all three individual Feynman amplitudes is observed in the wide region of the scattering angle besides near the two edges around $|\cos\theta_{W^-}| \approx 1$. We study in detail the LC gauge vector dependence of each amplitude in order to understand their behaviors shown in these figures.

We first note that the enhancement found for the contact interaction diagram, Fig. 10(c), which is given by red curves in Fig. 12, can only come from the two weak boson propagators attached to the final lepton pairs. The lepton current,

$$J^\mu = u_L(p_e)^\dagger \sigma_-^\mu v_L(p_{\bar{\nu}}) \quad (57)$$

can be expressed in general as a summation over three W boson helicity components as follows:

$$\begin{aligned} J^\mu &= \left(g^\mu{}_\nu - \frac{q^\mu q_\nu}{q^2} \right) J^\nu \\ &= \left(- \sum_{h=\pm 1, 0} \epsilon^\mu(q, h)^* \epsilon_\nu(q, h) \right) J^\nu \end{aligned}$$

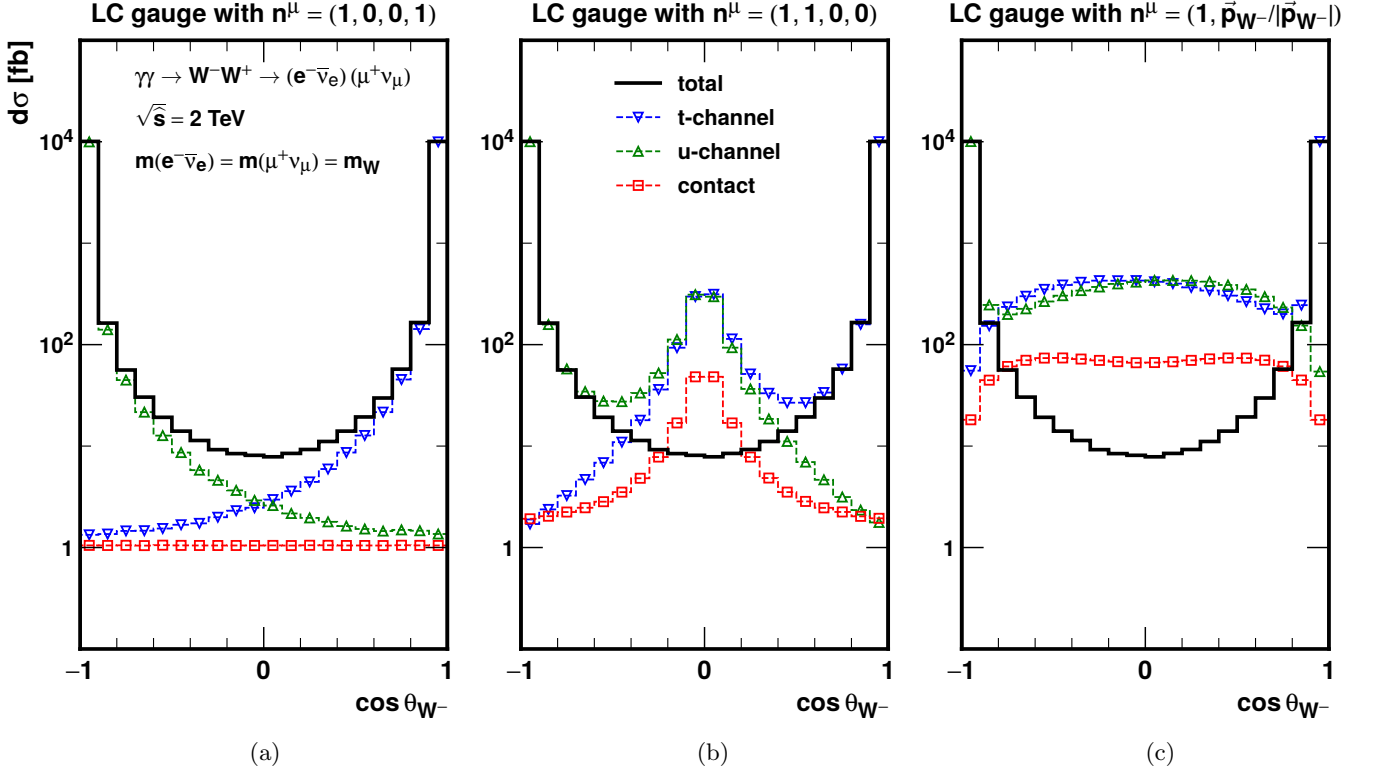


Fig. 12. Distribution of the scattering angle for $\gamma\gamma \rightarrow W^-W^+$ at $\sqrt{s} = 2$ TeV in the LC gauge with different LC vectors, when both W^+ and W^- are exactly on the mass shell.

$$= - \sum_{h=\pm 1,0} \epsilon^\mu(q, h)^* \epsilon(q, h) \cdot J, \quad (58)$$

where we assume zero lepton masses so that the current is conserved and has no Goldstone boson coupling. In the above expression, the term

$$\epsilon(q, h) \cdot J \quad (59)$$

gives Wigner's d -functions [35] in the rest frame of the decaying weak boson, or the splitting amplitudes [3] in boosted frames. Since the transverse polarization components $h = \pm 1$ do not grow with the weak boson energy, it is only the $h = 0$ component which grows with energy. In the Unitary gauge, or in an arbitrary covariant R_ξ gauge, it is this $h = 0$ component which grows with the weak boson energy. In the FD gauge, this $h = 0$ component is replaced by the $\tilde{\epsilon}^\mu(q, 0)$ term, whose magnitude decreases with energy.

Let us examine what happens to the $h = 0$ component of the leptonic current in the general LC gauge:

$$P_{LC}^{\mu\nu} \epsilon^\nu(q, 0) = P_{LC}^{\mu\nu} \left(\frac{q^\mu}{Q} + \tilde{\epsilon}^\nu(q, 0) \right). \quad (60)$$

For our example of $E_W = 1$ TeV, the magnitude of $\tilde{\epsilon}^\nu(q, 0)$ decreases by a factor of $e^{-\eta} \approx 0.04$ for $\cosh \eta = E_W/m_W$, and we can safely neglect its contribution against $q^\mu/Q \sim \mathcal{O}(E_W/m_W)$. Therefore, it is only the behavior of the scalar current term q^μ/Q we should examine.

We first note that the general LC gauge polarization tensor can be decomposed as

$$P_{LC}^{\mu\nu} = P_T^{\mu\nu} + q^2 \frac{n^\mu n^\nu}{(n \cdot q)^2}, \quad (61)$$

where the so-called ‘transverse’ polarization tensor satisfies

$$P_T^{\mu\nu} q_\mu = P_T^{\mu\nu} n_\nu = 0. \quad (62)$$

Because of the property (62), the scalar current component of the leptonic current reduces to

$$P_{LC}^{\mu\nu} \frac{q^\nu}{Q} = Q \frac{n^\mu}{n \cdot q}. \quad (63)$$

Since $Q \approx m_W$ around the resonance peak, and since n^μ is a constant gauge vector, it is the gauge term $n \cdot q$ in the denominator which we should examine.

Let us write down the four momentum of W^\pm in the colliding photon rest frame. We find

$$p_{W-}^\mu = (E_{W-}, p^* \sin \theta_{W-}, 0, p^* \cos \theta_{W-}) \quad (64a)$$

$$p_{W+}^\mu = (E_{W+}, -p^* \sin \theta_{W-}, 0, -p^* \cos \theta_{W-}) \quad (64b)$$

where

$$E_{W\pm} = \frac{\sqrt{s}}{2} \left(1 + \frac{p_{W\pm}^2 - p_{W\mp}^2}{s} \right) \quad (65)$$

and

$$p^* = \frac{\sqrt{s}}{2} \beta \left(\frac{p_{W-}^2}{s}, \frac{p_{W+}^2}{s} \right) \quad (66)$$

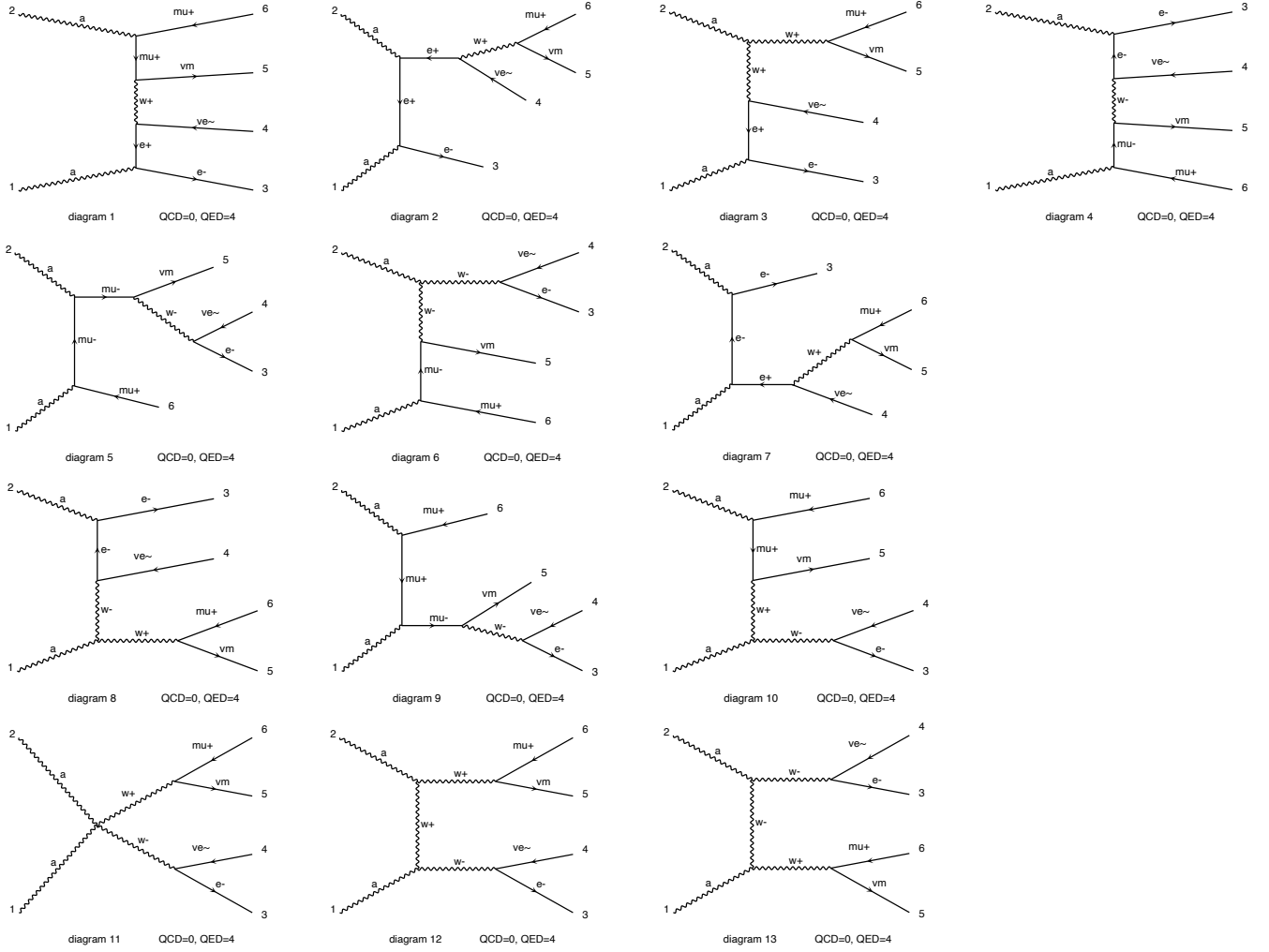


Fig. 13. Feynman diagrams for $\gamma\gamma \rightarrow e^- \bar{\nu}_e \mu^+ \nu_\mu$, generated by **Madgraph**.

with

$$\bar{\beta}(a, b) = \sqrt{1 - 2(a + b) + (a - b)^2} \quad (67)$$

is the common momentum of the W pair in the c.m. frame.

For the gauge vector (54a), the product is

$$n \cdot p_{W^\pm} = E_{W^\pm} \pm p^* \cos \theta_{W^\pm} \quad (68)$$

which can become small around $\cos \theta_{W^\pm} = \pm 1$, but after contracting all the four currents in the contact-term amplitudes Fig.10(c), the gauge terms proportional to n^μ cancel out: They vanish in the product of the W^- and W^+ currents because of $n \cdot n = 0$, whereas the product of W^\pm and the initial photon polarization vectors vanish, since

$$n \cdot \epsilon(p_\gamma, \pm 1) = 0 \quad (69)$$

for both photons with momenta along the z-axis.

In case of the gauge vector (54b), we find

$$n \cdot p_{W^\pm} = E_{W^\pm} \pm p^* \sin \theta_{W^\pm} \quad (70)$$

and one of which can be small at $\cos \theta_{W^\pm} \approx 0$. In the contact interaction amplitude, the enhanced current survives when contracted with the initial photon polarization

vectors, because

$$|n \cdot \epsilon(p_\gamma, \pm 1)| = |-\epsilon(p_\gamma, \pm 1)^1| = \frac{1}{2} \quad (71)$$

for both photons. The enhancement in the red histogram around $\cos \theta_{W^-} \approx 0$ observed in Fig. 12(b) is hence due to the LC gauge term.

Finally, for the gauge vector of (54c), we find

$$n \cdot p_{W^\pm} = E_{W^\pm} \pm p^* \quad (72)$$

which is independent of $\cos \theta_{W^\pm}$. In fact, the above term grows with energy for the W^+ propagator, because the three-vector direction $\vec{n} = \vec{p}_{W^-} / |\vec{p}_{W^-}|$ is opposite of the W^+ momentum direction in the c.m. frame, which is the prescription for the FD gauge. It is hence only the W^- propagator whose gauge term can grow with energy. Because the enhancement factor in the W^- propagator is independent of the scattering angle, we observe broad enhancement in Fig. 12(c). The enhancement effect diminishes near $\cos \theta_{W^\pm} = \pm 1$, because the gauge vector becomes orthogonal to one of the incoming photon polarization vectors in the limits.

Although we understand the gauge artefacts observed for the contact interaction term as above, we find that

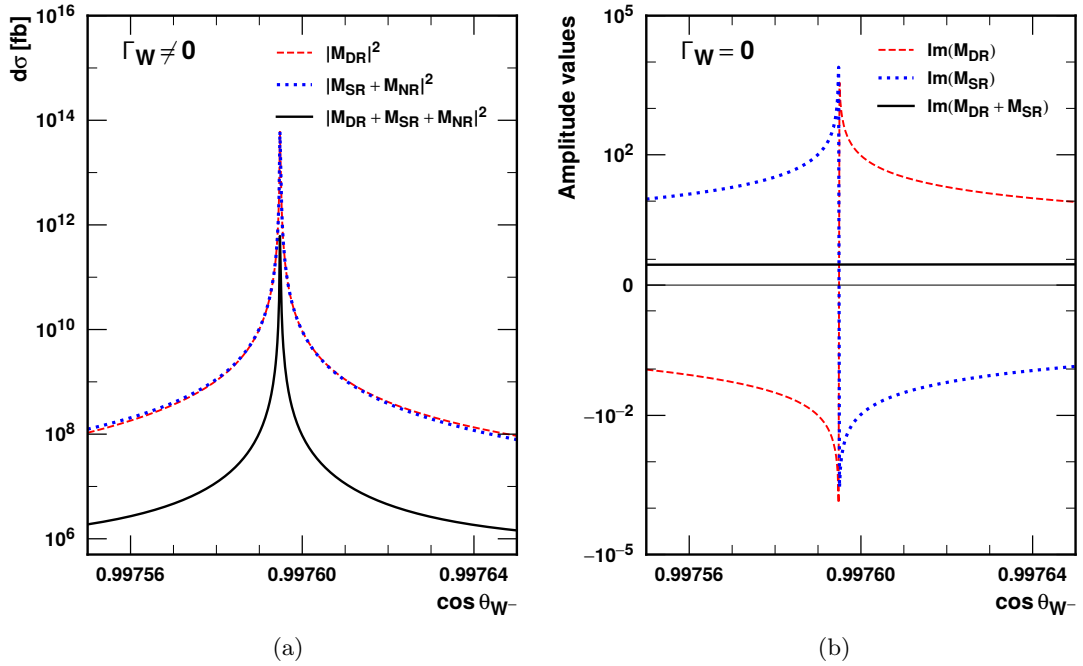


Fig. 14. (a) Differential cross section $d\sigma/d\cos\theta_{W-}$ for the process $\gamma\gamma \rightarrow e^-\bar{\nu}_e\mu^+\nu_\mu$ at $\sqrt{s} = 2$ TeV in the LC gauge with $n^\mu = (1, \sin\theta_{W-}, 0, \cos\theta_{W-}) = (1, \vec{p}_{W-}/|\vec{p}_{W-}|)$, where θ_{W-} is the polar angle of the $e^-\bar{\nu}_e$ pair. The invariant masses of the lepton pair are fixed at $m(\mu^+\nu_\mu) = 69.3$ GeV and $m(e^-\bar{\nu}_e) = m_W$. The red dashed curve shows the contribution of the three double resonant diagrams (\mathcal{M}_{DR}), while the blue dotted curve shows the contribution of all the other diagrams, single resonant (\mathcal{M}_{SR}) or non-resonant (\mathcal{M}_{NR}). The black solid curve shows the sum of all 13 Feynman diagrams. (b) Imaginary part of the amplitudes when the photon helicities are $\lambda_1 = \lambda_2 = -1$ and e^- and μ^+ momenta are along the $W^+(\mu^+\nu_\mu)$ momentum direction in the $\gamma\gamma$ rest frame. We set $\Gamma_W = 0$ in the off-shell W^- propagator.

the most serious problem arises in the t - and u -channel exchange amplitudes, from their gauge terms. The four momentum of the weak boson exchanged in the t -channel can be expressed as follows:

$$\begin{aligned} q^\mu &= p^\mu(\gamma_1) - p^\mu(W^-) \\ &= (E - E_{W-}, -p^* \sin\theta_{W-}, 0, E - p^* \cos\theta_{W-}) \end{aligned} \quad (73)$$

with $E = \sqrt{s}/2$. Let us show the gauge term for our three gauge vectors. For (54a), we find

$$n \cdot q = -(E_{W-} - p^* \cos\theta_{W-}). \quad (74)$$

This term can never vanish as long as both W^\pm invariant mass is in the resonance region. For (54b), we find

$$n \cdot q = E - E_{W-} + p^* \sin\theta_{W-}. \quad (75)$$

When both W 's are on-shell, $E_{W-} = E$, and hence the gauge term vanishes at $\sin\theta_{W-} = 0$, or at $\cos\theta_{W-} = \pm 1$. Once the invariant mass of W^- is larger than that of W^+ , the zero appears in the physical region. Although the LC gauge pole singularity can be integrated out in loop calculation e.g. by taking the principal value integral [34], once the pole appears in the physical region of the phase space integral, the MC integral fails instantly, since the singular terms appear in the absolute value square of the amplitudes.

Let us study how the LC gauge pole singularity appears in the resonant amplitudes, and how they are cancelled in the physical amplitudes, by using the gauge vector (54c). The four momentum of the W boson exchanged

in the t -channel is given by eq. (73) and the gauge term for (54c) becomes

$$n \cdot q = E - E_{W-} + p^* - E \cos\theta_{W-}. \quad (76)$$

The $n \cdot q = 0$ pole can appear at

$$\cos\theta_{W-} = (E - E_{W-} + p^*)/E. \quad (77)$$

When both W 's are on-shell, this happens at

$$\cos\theta_{W-} = \sqrt{1 - (m_W/E)^2}, \quad (78)$$

which is 0.9968 at $\sqrt{s} = 2$ TeV. We find, however, that this pole does not show up in the amplitudes because each on-shell amplitude vanishes exactly at the corresponding pole.

We find that the above vanishing of individual Feynman amplitude at the pole of the LC gauge term does not hold when one or both of the weak bosons is off-shell. There appear non-zero amplitudes which are proportional to the off-shellness of decaying W 's, $(m(e^-\bar{\nu}_e)^2 - m_W^2)$ and/or $(m(\mu^+\nu_\mu)^2 - m_W^2)$, as residues of the pole term. We further find that the singular terms do not cancel even after summing up the three resonant diagrams of Figs. 10(a),(b),(c).

We therefore evaluate all the 13 diagrams contributing to the process

$$\gamma\gamma \rightarrow e^-\bar{\nu}_e\mu^+\nu_\mu \quad (79)$$

as shown in Fig. 13, generated by **MadGraph** [17–19]. We note that the three double resonant (DR) diagrams of

Fig. 10 are now labeled as 11, 12, 13 at the bottom of Fig. 13. The diagrams 2, 3, 7, 8 have W^+ propagator, while the diagrams 5, 6, 9, 10 have W^- propagator only, and we call them single resonant (SR) diagrams. The diagrams 1 and 4 have no W^\pm propagator, and are labeled as non-resonant (NR).

$$\text{In Fig. 14(a), we show the } \cos\theta_{W^-} \text{ distribution when}$$

$$m(e^-\bar{\nu}_e) = 69.3 \text{ GeV} \approx m_W - 5.3 \Gamma_W, \quad (80a)$$

$$m(\mu^+\nu_\mu) = m_W = 80.4 \text{ GeV}, \quad (80b)$$

at $\sqrt{s} = 2 \text{ TeV}$. The red dashed curve shows the contribution of the sum of the three double resonant amplitudes,

$$|\mathcal{M}_{\text{DR}}|^2 = \left| \sum_{k=11}^{13} \mathcal{M}_k \right|^2. \quad (81)$$

Shown by the blue dashed curve is for the sum of all the other amplitudes

$$|\mathcal{M}_{\text{SR}} + \mathcal{M}_{\text{NR}}|^2 = \left| \sum_{k=1}^{10} \mathcal{M}_k \right|^2, \quad (82)$$

which sum over the 8 single resonant and 2 non-resonant amplitudes. We can tell from the red and blue dashed curves that they have the same singular behavior at $\cos\theta_{W^-} \approx 0.9976$, which is the pole position of eq. (77) for the invariant masses of eq. (80). Although the red and blue dashed curves in Fig. 14(a) confirm that the sum of the three double-resonant amplitudes (\mathcal{M}_{DR}) and that of the single and non-resonant amplitudes ($\mathcal{M}_{\text{SR}} + \mathcal{M}_{\text{NR}}$) have the same singular behavior, we find that the total sum of all the 13 diagrams in Fig. 13,

$$|\mathcal{M}_{\text{DR}} + \mathcal{M}_{\text{SR}} + \mathcal{M}_{\text{NR}}|^2 = \left| \sum_{k=1}^{13} \mathcal{M}_k \right|^2 \quad (83)$$

still gives the singular behavior, as shown by the black solid curve in the same plot. The magnitude of the singular term is significantly reduced, and hence there is a hint of cancellation among the 13 amplitudes of Fig. 13.

We find that this non-cancellation of the LC gauge pole singularity is due to the width term in the W boson propagator, unitarized by the Breit-Wigner prescription [36]. At the kinematical point on top of the pole, $n \cdot p_W = 0$, the non-vanishing off-shell amplitudes are proportional to $p_W^2 - m_W^2$. This term cancels the W propagator factor exactly, only if the width is set to be zero. In the presence of the finite width term, the cancellation is not exact, and the pole singularity in the resonant amplitudes survive even after summing over all the non-resonant amplitudes.

In order to demonstrate cancellation of the LC gauge pole singularity between the resonant and non-resonant amplitudes, we show in Fig. 14(b) the amplitude of the double resonant diagrams, and that of the single W^+ resonant diagrams for the lepton-pair invariant masses of eq. (76). We show only the amplitude when both incoming photons are left-handed ($\lambda_{\gamma_1} = \lambda_{\gamma_2} = -1$), and when the final e^- and μ^+ momenta are along the W^+ ($\mu^+\nu_\mu$) momentum direction. With this set up the double resonant amplitude is proportional to the helicity amplitude for

$$\gamma_1(-1) + \gamma_2(-1) \rightarrow W^+(+1) + W^-(+1), \quad (84)$$

where ± 1 inside parentheses denote helicities. We keep the width factor of the W^+ propagator so that the amplitude is finite and pure imaginary on top of the W^+ boson mass shell, (80b). We set the width of off-shell W^- propagator to zero, in order to demonstrate the cancellation of the LC gauge pole singularities between the double resonant amplitudes ($\mathcal{M}_{\text{DR}} = \mathcal{M}_{11} + \mathcal{M}_{12} + \mathcal{M}_{13}$) and the single W^+ resonant amplitudes ($\mathcal{M}_{\text{SR}} = \mathcal{M}_2 + \mathcal{M}_3 + \mathcal{M}_7 + \mathcal{M}_8$). These amplitudes are pure imaginary (due to on-shell W^+), and we show the imaginary part of \mathcal{M}_{DR} by the red-dashed line, that of \mathcal{M}_{SR} by the blue-dashed line, and their sum by the black line. We can clearly observe exact cancellation of the LC gauge pole singularity between the \mathcal{M}_{DR} and the \mathcal{M}_{SR} amplitudes. Similar cancellation takes place in the real part of the amplitudes between the W^- SR amplitudes and NR amplitudes, with significantly smaller magnitudes.

The apparent LC gauge vector dependence of the amplitudes is hence the artefact of the Breit-Wigner unitarization [36] of the W boson propagator, which violates the order-by-order gauge invariance of the perturbative amplitudes.

Since it is not practical to sum up all the non-resonant amplitudes before unitarizing the resonant W amplitudes, we propose that the LC gauge vector should be carefully chosen such that the LC gauge term does not have a pole in the physical region of all the contributing gauge boson propagators. Among our examples, the choice (54a) should be safe, as long as the final state particles are massive or has large p_T .

5 Summary

In this report, we show that the FD gauge propagators introduced in refs. [1, 2] can be obtained from the LC gauge propagators, or the Green's functions of the equation of motion (EOM) of the free gauge fields in the LC gauge, not only in QED and QCD, but also in the EW theory with massive weak bosons. In particular, the 5×5 representation of the weak boson propagators is directly obtained from the EOM of the free weak boson and its associate Goldstone boson fields in the LC gauge. The FD gauge propagators are then obtained simply by choosing the LC gauge vector along the opposite direction of the three-momentum of the off-shell gauge boson.

Because the general LC gauge propagators and the scattering amplitudes have identical form as those in the FD gauge, we modify the new HELAS codes [1, 2] to allow an arbitrary LC gauge vector which is common among all the propagators in the amplitudes. With this minimum modification of the programs developed in refs. [1] and [2], we are able to obtain helicity amplitudes of all the SM processes in an arbitrary LC gauge.

Since helicity amplitudes for all $2 \rightarrow 2$ processes are gauge invariant in QED and QCD, we have studied a few $2 \rightarrow 3$ processes, $\ell\bar{\ell}' \rightarrow \ell\bar{\ell}'\gamma$, $\ell\ell' \rightarrow \ell\ell'\gamma$ and $gg \rightarrow ggg$, in section 3. We find that LC gauge amplitudes don't improve cancellation among diagrams in general, because only when the LC gauge vector orientation is along or

approximately along the FD gauge vector of a particular current, the off-shell current components proportional to its four momentum are suppressed. We note that a specific choice of the LC gauge vector gives soft gluon radiation patterns efficiently, confirming the observation in parton shower studies [9, 10].

In case of the EW theory amplitudes, $2 \rightarrow 2$ processes like $\gamma\gamma \rightarrow W^+W^-$ have gauge dependence, and we study the amplitudes in detail in section 4. We confirm that, just like in the FD gauge, the LC gauge amplitudes are free from subtle cancellation among interfering amplitudes [32] which are unavoidable in all covariant gauges, including R_ξ and Unitary gauges. We also find that we should choose the LC gauge vector cautiously, such that no pole due to the vanishing gauge term, $n \cdot q = 0$, should appear in the physical region of any of the gauge boson propagators.

From the perspective of high energy computation tools development, our LC gauge quantization approach has an absolute advantage over the previously proposed method [2] of modifying the amplitudes generated in the Unitary or R_ξ gauges. If we start from the Unitary gauge, as in ref. [2], although the number of Feynman diagrams can be reduced due to the absence of the Goldstone boson propagation, some of the fundamental vertices like the four-point neutral Goldstone boson coupling are absent from the Feynman rule. As a consequence, the authors of ref. [2] added a few vertices to the SM interactions in order to generate appropriate Feynman diagrams and the corresponding amplitudes. If we start from the R_ξ gauge, things become even more complicated. It is because all the Goldstone boson propagators should first be cancelled against the corresponding R_ξ gauge boson propagators which share the same four momentum, by using the BRST identities. At this stage, all the amplitudes with the Goldstone boson propagators are removed, and the vertices which are missing in the Unitary gauge should be re-introduced. Although there are only four such vertices in the SM of the EW theory [2], we anticipate more missing vertices, in models beyond the SM or even in the SM effective field theory (SMEFT).

On the other hand, in the LC gauge quantization of the weak bosons, no unphysical particles propagates because all the Goldstone bosons are the 5th component of the corresponding physical weak bosons. The Feynman rules are then straightforward, since we do not distinguish the first 4 and the 5th components of the weak bosons when generating Feynman diagrams. All the vertices are straightforward to obtain once the Higgs sector of the model is specified. The method can be applied for all SMEFT operators, and for all BSM models with spontaneously broken gauge symmetries. We therefore believe that the next generation of scattering amplitude generators should adopt the LC gauge form of the massless and massive gauge boson propagators. The FD gauge amplitudes are then obtained by choosing the gauge vector along the opposite direction of each off-shell gauge boson momentum.

Acknowledgements

JK and YZ would like to thank KEK Theory Center for hospitality where part of the work is done. JMC is supported by Fundamental Research Funds for the Central Universities of China NO. 11620330. The work was supported in part by World Premier International Research Center Initiative (WPI Initiative), MEXT, Japan, and also by JSPS KAKENHI Grant No. 20H05239, 21H01077, 21K03583 and 23K03403.

References

1. K. Hagiwara, J. Kanzaki, and K. Mawatari, “QED and QCD helicity amplitudes in parton-shower gauge,” *Eur. Phys. J. C* **80** (2020) no. 6, 584, [arXiv:2003.03003 \[hep-ph\]](#).
2. J. Chen, K. Hagiwara, J. Kanzaki, and K. Mawatari, “Helicity amplitudes without gauge cancellation for electroweak processes,” *Eur. Phys. J. C* **83** (2023) no. 10, 922, [arXiv:2203.10440 \[hep-ph\]](#).
3. K. Hagiwara, Q. Li, and K. Mawatari, “Jet angular correlation in vector-boson fusion processes at hadron colliders,” *JHEP* **07** (2009) 101, [arXiv:0905.4314 \[hep-ph\]](#).
4. J. Chen, T. Han, and B. Tweedie, “Electroweak Splitting Functions and High Energy Showering,” *JHEP* **11** (2017) 093, [arXiv:1611.00788 \[hep-ph\]](#).
5. G. Cuomo, L. Vecchi, and A. Wulzer, “Goldstone Equivalence and High Energy Electroweak Physics,” *SciPost Phys.* **8** (2020) no. 5, 078, [arXiv:1911.12366 \[hep-ph\]](#).
6. A. Wulzer, “An Equivalent Gauge and the Equivalence Theorem,” *Nucl. Phys. B* **885** (2014) 97–126, [arXiv:1309.6055 \[hep-ph\]](#).
7. M. S. Chanowitz and M. K. Gaillard, “The TeV Physics of Strongly Interacting W’s and Z’s,” *Nucl. Phys. B* **261** (1985) 379–431.
8. H. G. J. Veltman, “The Equivalence Theorem,” *Phys. Rev. D* **41** (1990) 2294.
9. Z. Nagy and D. E. Soper, “Parton showers with quantum interference,” *JHEP* **09** (2007) 114, [arXiv:0706.0017 \[hep-ph\]](#).
10. Z. Nagy and D. E. Soper, “A parton shower based on factorization of the quantum density matrix,” *JHEP* **06** (2014) 097, [arXiv:1401.6364 \[hep-ph\]](#).
11. C. Becchi, A. Rouet, and R. Stora, “Renormalization of Gauge Theories,” *Annals Phys.* **98** (1976) 287–321.
12. I. V. Tyutin, “Gauge Invariance in Field Theory and Statistical Physics in Operator Formalism,” [arXiv:LEBEDEV-75-39 \[hep-th\]](#).
13. G. J. Gounaris, R. Kogerler, and H. Neufeld, “Relationship Between Longitudinally Polarized Vector Bosons and their Unphysical Scalar Partners,” *Phys. Rev. D* **34** (1986) 3257.
14. K. Fujikawa, B. W. Lee, and A. I. Sanda, “Generalized Renormalizable Gauge Formulation of Spontaneously Broken Gauge Theories,” *Phys. Rev. D* **6** (1972) 2923–2943.
15. K. Hagiwara, H. Murayama, and I. Watanabe, “Search for the Yukawa interaction in the process $e^+e^- \rightarrow t\bar{t}Z$ at TeV linear colliders,” *Nucl. Phys. B* **367** (1991) 257–286.

16. H. Murayama, I. Watanabe, and K. Hagiwara, “HELAS: HELicity amplitude subroutines for Feynman diagram evaluations,” *KEK-91-11*.
17. T. Stelzer and W. F. Long, “Automatic generation of tree level helicity amplitudes,” *Comput. Phys. Commun.* **81** (1994) 357–371, [arXiv:hep-ph/9401258](#).
18. J. Alwall, M. Herquet, F. Maltoni, O. Mattelaer, and T. Stelzer, “MadGraph 5 : Going Beyond,” *JHEP* **06** (2011) 128, [arXiv:1106.0522 \[hep-ph\]](#).
19. J. Alwall, R. Frederix, S. Frixione, V. Hirschi, F. Maltoni, O. Mattelaer, H. S. Shao, T. Stelzer, P. Torrielli, and M. Zaro, “The automated computation of tree-level and next-to-leading order differential cross sections, and their matching to parton shower simulations,” *JHEP* **07** (2014) 079, [arXiv:1405.0301 \[hep-ph\]](#).
20. Z. Kunszt and D. E. Soper, “On the Validity of the Effective W Approximation,” *Nucl. Phys. B* **296** (1988) 253–289.
21. J. Ellis, “TikZ-Feynman: Feynman diagrams with TikZ,” *Comput. Phys. Commun.* **210** (2017) 103–123, [arXiv:1601.05437 \[hep-ph\]](#).
22. M. Dohse, “TikZ-FeynHand: Basic User Guide,” [arXiv:1802.00689 \[cs.OH\]](#).
23. K. Hagiwara, H. Iwasaki, A. Miyamoto, H. Murayama, and D. Zeppenfeld, “Single weak boson production at TeV e^+e^- colliders,” *Nucl. Phys.* **B365** (1991) 544–596.
24. R. W. Brown, K. L. Kowalski, and S. J. Brodsky, “Classical Radiation Zeros in Gauge Theory Amplitudes,” *Phys. Rev. D* **28** (1983) 624. [Addendum: *Phys.Rev.D* 29, 2100–2104 (1984)].
25. K. Hagiwara and T. Yamada, “Null radiation zone at the LHC,” *Phys. Rev. D* **87** (2013) no. 1, 014021, [arXiv:1210.0973 \[hep-ph\]](#).
26. K. Hagiwara, D. Marfatia, and T. Yamada, “Isospin-Violating Dark Matter at the LHC,” *Phys. Rev. D* **89** (2014) no. 9, 094017, [arXiv:1207.6857 \[hep-ph\]](#).
27. J. Pumplin, D. R. Stump, J. Huston, H. L. Lai, P. M. Nadolsky, and W. K. Tung, “New generation of parton distributions with uncertainties from global QCD analysis,” *JHEP* **07** (2002) 012, [arXiv:hep-ph/0201195](#).
28. Y. L. Dokshitzer, V. S. Fadin, and V. A. Khoze, “Coherent Effects in the Perturbative QCD Parton Jets,” *Phys. Lett. B* **115** (1982) 242–246.
29. A. Bassetto, M. Ciafaloni, G. Marchesini, and A. H. Mueller, “Jet Multiplicity and Soft Gluon Factorization,” *Nucl. Phys. B* **207** (1982) 189–204.
30. R. K. Ellis, G. Marchesini, and B. R. Webber, “Soft Radiation in Parton Parton Scattering,” *Nucl. Phys. B* **286** (1987) 643. [Erratum: *Nucl.Phys.B* 294, 1180 (1987)].
31. C. Dams and R. Kleiss, “The Electroweak standard model in the axial gauge,” *Eur. Phys. J. C* **34** (2004) 419–427, [arXiv:hep-ph/0401136](#).
32. S. Bailey and L. A. Harland-Lang, “Modeling W^+W^- production with rapidity gaps at the LHC,” *Phys. Rev. D* **105** (2022) no. 9, 093010, [arXiv:2201.08403 \[hep-ph\]](#).
33. **Particle Data Group** Collaboration, R. L. Workman *et al.*, “Review of Particle Physics,” *PTEP* **2022** (2022) 083C01.
34. G. Leibbrandt, “Introduction to Noncovariant Gauges,” *Rev. Mod. Phys.* **59** (1987) 1067.
35. E. P. Wigner, “On Unitary Representations of the Inhomogeneous Lorentz Group,” *Annals Math.* **40** (1939) 149–204.
36. G. Breit and E. Wigner, “Capture of Slow Neutrons,” *Phys. Rev.* **49** (1936) 519–531.